Journal of Computational Physics **178,** 81–117 (2002)
doi:10.1006/jcph.2002.7021, available online at http://www.idealibrary.com on IDEAL®

Conservative Hybrid Compact-WENO Schemes for Shock-Turbulence Interaction

Sergio Pirozzoli[1]

Università degli Studi di Roma "La Sapienza," Dipartimento di Meccanica e Aeronautica, Via Eudossiana 18, 00184 Rome, Italy
E-mail: piros@grasso.ing.uniromal.it

Received August 27, 2001; revised February 13, 2002

In the present paper an efficient hybrid compact-WENO scheme is proposed to obtain high resolution in shock-turbulence interaction problems. The algorithm is based on a fifth-order compact upwind algorithm in conservation form to solve for the smooth part of the flow field, which is coupled with a high-resolution weighted essentially nonoscillatory (WENO) scheme to capture the discontinuities. The derivation of the compact scheme is discussed in detail, and a stability study of the full discretization is included. The performance of the numerical algorithm has been assessed by performing preliminary simulations on benchmark problems, such as the interaction of a shock wave with entropy and vortical disturbances. The algorithm here developed is proven to have better resolution properties than standard WENO schemes and hybrid compact-ENO schemes as well, at a lower computational cost. In addition, the application to more realistic shock-turbulence interaction problems is discussed.

Key Words: compact schemes; shock-capturing schemes; shock-turbulence interaction.

1. INTRODUCTION

Direct numerical simulations of turbulence and large-eddy simulations require the use of highly accurate numerical schemes, which must be capable of resolving a very broad range of length scales that are often orders of magnitude apart. For this purpose compact methods have been developed which guarantee spectral-like resolution properties, are cheaper to use than spectral and pseudospectral schemes, and are easier to handle, especially when nontrivial geometries are involved. The interest in compact schemes for turbulence and aeroacoustics simulations seems to have started from the pioneering work of Lele [28],

[1] Fax: +39 06 4881759.

0021-9991/02 $35.00

even though compact approximations have been used previously by other authors (see, for example, Refs. [9, 25]). Lele developed compact approximations for first and second derivatives in the framework of a finite-difference approach and extensively applied the method of Fourier analysis (discussed in great detail in Ref. [45]) to analyze the errors involved with difference approximations. Indeed, the order of the truncation error of a numerical scheme provides information on the asymptotic convergence rate to the exact solution, but it does not provide any information on the spectrum of the truncation error. As a result of this type of analysis, the dispersion-relation-preserving (DRP) finite-difference schemes have been developed [42]. The basic idea of those schemes is to optimize the coefficients of the compact scheme to improve their resolution properties (i.e., their behavior in Fourier space) in order to resolve with high accuracy waves whose wavelength is small with respect to the computational grid (i.e., which are resolved with a few number of points per wavelength). The schemes presented in Refs. [28, 42] are intrinsically nondissipative, as central differences are used to approximate the derivatives. However, a small amount of numerical dissipation is often necessary in practical applications in order to damp out oscillations issuing from initial and boundary conditions, as well as from aliasing error. For this purpose compact upwind schemes have been developed [1, 44, 49], which drop the restriction of symmetric coefficients, thus allowing the scheme to be upwind even with a centered stencil. The introduction of upwinding introduces an amount of dissipation which is limited to high wavenumbers and can be adjusted by a careful design of the scheme. Recently, finite-volume compact schemes have also been attempted [14, 24]. The latter authors have demonstrated that a conservative formulation, in addition to having inherent advantages for the computation of compressible flows [21], also provides better resolution properties with respect to a nonconservative approach.

It is well-known that for problems involving discontinuities, fixed-stencil explicit and compact approximations (of second order or higher) necessarily produce oscillations whose amplitude does not decrease as the grid is refined (the latter phenomenon is referred to as the Gibbs phenomenon). Such oscillations are usually unacceptable if an accurate solution is required, such as for direct simulation of shock-turbulence interaction. Several approaches have been proposed to overcome this difficulty. An original idea was proposed by Cockburn and Shu [8], who employed a TVB limiter to stabilize compact (central and upwind) schemes. The latter approach was proven to be able to yield oscillation-free solutions when applied the the Burgers equation. More recently, weighted essentially nonoscillatory (WENO) schemes have been developed as a follow-up of the classical essentially nonoscillatory (ENO) schemes, originally developed by Harten *et al*. [20]. The formulation of the WENO schemes has been discussed in detail in several papers in recent years [22, 30, 39], and such schemes have been used successfully in applications [17, 33]. WENO schemes have the advantage over the ENO ones to yield higher order accuracy for the same stencil size, and at the same time to cure the well-known order degeneracy phenomenon of the ENO schemes related to the free stencil adaptation in smooth regions [36, 38]. However, those shock-capturing schemes are usually not optimal for computing turbulent flows or for aeraocoustics applications, because they exhibit poor resolution qualities compared to linear compact schemes. For this reason there have been a number of efforts in recent years to try to overcome the deficiency of conventional shock-capturing schemes in computing shock-turbulence interaction problems, where small scales can be seriously damped by the numerical dissipation which is necessary to properly resolve shock waves. An interesting attempt is the one undertaken by Adams and Shariff [1]. Those authors have developed

hybrid schemes that rely on the coupling of a nonconservative compact upwind scheme with a shock-capturing ENO scheme that is turned on around discontinuities. Two types of optimized compact schemes were developed in [1] which exhibit different levels of numerical dissipation, and which both require the inversion of a pentadiagonal matrix. The coupling between the compact and the ENO scheme was efficiently performed by precomputing the node-based flux derivatives by ENO at critical cells. The results presented in Ref. [1] clearly indicate that hybrid schemes combine the advantages of compact schemes in smooth regions with a sharp representation of discontinuities and thus are good candidates for efficiently computing shock-turbulence interaction problems. The same algorithm has been successfully applied for the direct numerical simulation of a turbulent compression ramp flow [2]. A different approach was devised by Deng and Maekawa [11]; those authors developed nonlinear compact schemes based on an adaptive mechanism of selection among different compact stencils based on the smoothness properties of the function to interpolate. Deng and Zhang [12] developed an algorithm whereby the resolution properties of WENO schemes are improved by introducing compact approximations for pointwise derivatives rather than explicit ones. Recently there have been attempts to improve the resolution properties of WENO schemes; some of them [46, 47] are based on the attempt to relax the requirements on the formal order of accuracy of the scheme to achieve better resolution properties at high frequencies. Some others are based on the substitution of polynomial-explicit reconstructions with compact approximations [23].

In the present paper we follow the same basic approach proposed in Ref. [1] to derive a hybrid compact-WENO scheme. However, our effort has been to improve some features of the scheme. First, a conservative approach for the compact scheme is developed rather than a nonconservative one; this feature makes coupling with the shock-capturing scheme easier than in the original formulation and is shown to cause a lower level of numerical oscillations than is found in Ref. [1]. Second, the compact algorithm is based on the inversion of a tridiagonal matrix rather than a pentadiagonal one, which makes the scheme more efficient from a computational standpoint, while retaining (at least) the same resolution properties as the schemes developed in Ref. [1]. Finally, a weighted ENO scheme is used to resolve discontinuities rather than an ENO one. Indeed it is shown that the overall performance of hybrid schemes in computing shock-turbulence interaction problems is critically affected by the order of accuracy of the shock-capturing scheme that is employed. WENO schemes therefore represent a better candidate than ENO schemes, as they yield better accuracy properties virtually at the same price. Evidence of the nice features of the hybrid compact-WENO scheme is given in the paper by performing a number of benchmark simulations, which indeed confirm a performance of the present formulation of hybrid scheme better than the original formulation of Ref. [1]. A more realistic application is also presented, consisting of the computation of a three-dimensional shock-turbulence interaction problem.

The paper is organized as follows. In Section 2 a conservative compact upwind scheme is formulated, and a detailed discussion of the implementation of proper boundary conditions and a stability analysis of the fully discretized scheme is presented; a convergence study for smooth solutions will also be presented. In Section 3 the formulation of the WENO algorithm is briefly discussed, with an emphasis on the coupling with the compact scheme, and a computational study on the linear advection equation with discontinuous initial conditions is included. In Section 4 the algorithm is extended to deal with the full nonlinear Euler equations of gasdynamics. Finally, in Section 5 the hybrid scheme is applied to a number of benchmark test cases, as well as to a shock-turbulence interaction problem.

2. FORMULATION OF A CONSERVATIVE COMPACT UPWIND FINITE-DIFFERENCE SCHEME

In the present section we describe the formulation of a class of compact upwind finite-difference schemes in the framework of a conservative approach. Such a scheme is intended to be applied in the smooth regions of the flow field, and in order to achieve a shock-capturing capability, it is coupled with a weighted ENO scheme, as explained in the next section. Compact schemes have several advantages over their noncompact counterparts: (i) for the same number of points in the stencil they yield better accuracy and resolution properties [1, 28]; (ii) the operation count varies linearly with the number of grid points, as in the explicit case, as compact schemes involve the inversion of narrowly banded matrices; and (iii) the implementation of boundary conditions is made easier because fewer boundary points must be handled. These properties have been discussed in detail in Ref. [28] for central compact difference schemes. In the present work we describe the derivation of conservative compact upwind schemes, in a fashion similar to what has been done for central schemes in [14] and [24]. A conservative approximation of the derivatives that appear in conservation equations is necessary when discontinuities in the flow field occur, because then the Lax–Wendroff theorem holds [29], which guarantees that the latter propagate at the correct speed. Of course, the proper tracking of flow discontinuities is guaranteed by selectively applying the weighted ENO algorithm close to the shocks themeselves; however, we argue that using a conservative approximation throughout the computational domain is more sound and also allows a better coupling with the weighted ENO algorithm. This claim is substantiated in the Results section.

The problem under consideration is the formulation of a conservative approximation to the derivative of a scalar variable $v(x)$ starting from its pointwise values (i.e., in a finite-difference approach), and exploiting compact approximants. Let the pointwise values of $v(x)$ be given on a set of grid points

$$v_i = v(x_i), \quad i = 1, 2, \ldots, N, \tag{1}$$

where N is the number of grid points, and let h be the grid spacing, which is assumed to be uniform. The problem is to determine a numerical flux function $\tilde{v}_{i+1/2}$ such that the difference of the fluxes at the intermediate nodes $i + 1/2$ and $i - 1/2$ yields a kth order approximation to the derivative $v'(x_i)$:

$$\frac{1}{h}\left(\tilde{v}_{i+1/2} - \tilde{v}_{i-1/2}\right) = v'(x_i) + O(h^k), \quad i = 1, \ldots, N. \tag{2}$$

It can be shown [20] that this problem is equivalent to an interpolation problem whereby the reconstructions of a scalar variable $u(x)$ at the intermediate nodes $\tilde{u}_{i+1/2}$ are evaluated starting from its cell-average values

$$\bar{u}_i = \frac{1}{h}\int_{x_{i-1/2}}^{x_{i+1/2}} u(x)\,\mathrm{d}x,$$

with the following identification:

$$\tilde{v}_{i+1/2} = \tilde{u}_{i+1/2}, \quad v_i = \bar{u}_i. \tag{3}$$

In particular, it can be shown that in order for (2) to be satisfied, it is sufficient to have

$$\tilde{u}_{i+1/2} = u_{i+1/2} + O(h^k).$$

Let us look for a compact (implicit) representation of the reconstruction of $u(x)$ around the intermediate node $i + 1/2$,

$$\sum_{l=-L_1}^{L_2} \alpha_l \tilde{u}_{i+1/2+l} = \sum_{m=-M_1}^{M_2} a_m \bar{u}_{i+m}, \tag{4}$$

or else

$$\sum_{l=-L_1}^{L_2} \alpha_l \tilde{v}_{i+1/2+l} = \sum_{m=-M_1}^{M_2} a_m v_{i+m}. \tag{5}$$

Assuming that the function u can be expanded in Taylor series up to order K around $x_{i+1/2}$,

$$u(x) = \sum_{n=0}^{K-1} u_{i+1/2}^{(n)} \frac{\left(x - x_{i+1/2}\right)^n}{n!} + O(h^K),$$

and recalling that

$$\bar{u}_{i+m} = \frac{U_{i+m+1/2} - U_{i+m-1/2}}{h},$$

where $U(x)$ is the primitive function of $u(x)$,

$$U(x) = \sum_{n=0}^{K-1} u_{i+1/2}^{(n)} \frac{\left(x - x_{i+1/2}\right)^{n+1}}{(n+1)!} + O(h^{K+1}),$$

we thus obtain

$$\bar{u}_{i+m} = \sum_{n=0}^{K-1} u_{i+1/2}^{(n)} \frac{1}{(n+1)!} [m^{n+1} - (m-1)^{n+1}] h^n + O(h^{K+1}).$$

Inserting the Taylor expansions of u and $\bar{u}$ into Eq. (4), and matching the coefficients of like powers of h, requiring the approximation to be kth order accurate (with $k \leq K$) one easily arrives at

$$(n+1) \sum_{l=-L_1}^{L_2} \alpha_l l^n - \sum_{m=-M_1}^{M_2} a_m [m^{n+1} - (m-1)^{n+1}] = 0, \quad n = 0, \ldots, k-1. \tag{6}$$

The coefficients for the compact upwind scheme can then be obtained by solving the system of Eqs. (6) with respect to the coefficients α_l ($L_1 + L_2 + 1$ unknowns) and a_m ($M_1 + M_2 + 1$ unknowns). Note that such coefficients are not independent (for example one can set $\alpha_{L_2} = 1$), and as a consequence there are only $L_1 + L_2 + M_1 + M_2 + 1$ independent unknowns. If the required order of accuracy is $k \leq L_1 + L_2 + M_1 + M_2 + 1$ the system

(6) is solvable, and $L_1 + L_2 + M_1 + M_2 + 1 - k$ free coefficients are left. In the present work we are interested in compact upwind interpolations with a narrow stencil so as to use efficient matrix inversion algorithms, such as the Thomas algorithm. In particular, we consider the case $L_1 = L_2 = M_1 = M_2 = 1$, which only implies the inversion of a tridiagonal matrix. A two-parameter class of third-order compact upwind schemes can then be obtained by requiring $k = 3$ and choosing α_0 and α_{-1} as free coefficients,

$$\alpha_1 = 1; \quad a_{-1} = \frac{1}{3} + \frac{\alpha_{-1}}{3} - \frac{\alpha_0}{6}, \quad a_0 = -\frac{7}{6} + \frac{5\alpha_{-1}}{6} + \frac{5\alpha_0}{6}, \quad a_1 = \frac{11}{6} - \frac{\alpha_{-1}}{6} + \frac{\alpha_0}{3};$$

in the same way a one-parameter family of fourth-order schemes is obtained by requiring $k = 4$ and taking α_0 as a free coefficient,

$$\alpha_{-1} = \alpha_0 - 3, \quad \alpha_1 = 1; \quad a_{-1} = -\frac{2}{3} + \frac{\alpha_0}{6}, \quad a_0 = -\frac{11}{3} + \frac{5\alpha_0}{3}, \quad a_1 = \frac{7}{3} + \frac{\alpha_0}{6}.$$

The only fifth-order compact upwind scheme in the class is obtained for $k = 5$, yielding the following interpolation scheme:

$$3\tilde{u}_{i-1/2} + 6\tilde{u}_{i+1/2} + \tilde{u}_{i+3/2} = \frac{1}{3}\bar{u}_{i-1} + \frac{19}{3}\bar{u}_i + \frac{10}{3}\bar{u}_{i+1}. \tag{7}$$

Recalling the identification (3) it is finally possible to revert to a conservative finite-difference formulation, and write down for the reconstruction at the intermediate nodes the approximation

$$3\tilde{v}_{i-1/2} + 6\tilde{v}_{i+1/2} + \tilde{v}_{i+3/2} = \frac{1}{3}v_{i-1} + \frac{19}{3}v_i + \frac{10}{3}v_{i+1}, \tag{8}$$

which, when inserted into Eq. (2), yields a fifth-order approximation to the first derivative of v. It is important to point out that Eq. (8) is also suitable for practical implementation of the scheme, since the matrix to invert is diagonally dominant, which is a sufficient condition for the Thomas algorithm to be stable. It must also be pointed out that the numerical flux function defined by Eq. (8) is not a local function of v_i due to the inversion of a tridiagonal matrix. Nevertheless it can be shown [5] that the Lax–Wendroff theorem still holds for such an approximation.

In the same way, explicit approximations can be constructed by choosing $L_1 = L_2 = 0$ and $M_1 = M_2 = 2$, which yields the explicit fifth-order, upwind-biased scheme

$$\tilde{v}_{i+1/2} = \frac{1}{30}v_{i-2} - \frac{13}{60}v_{i-1} + \frac{47}{60}v_i + \frac{9}{20}v_{i+1} - \frac{1}{20}v_{i+2}, \tag{9}$$

or $M_1 = M_2 = 3$, which yields the seventh-order-accurate scheme

$$\tilde{v}_{i+1/2} = -\frac{1}{140}v_{i-3} + \frac{5}{84}v_{i-2} - \frac{101}{420}v_{i-1} + \frac{319}{420}v_i + \frac{107}{210}v_{i+1} - \frac{19}{210}v_{i+2} + \frac{1}{105}v_{i+3}. \tag{10}$$

The latter formulas are important, as the fifth-order and the seventh-order WENO schemes later discussed reduce to (9) and (10) in smooth regions.

2.1. Resolution Properties

In order to investigate the resolution properties of finite-difference approximations it is customary to consider the linear advection equation [45]

$$v_t + a v_x = 0, \quad a > 0, \tag{11}$$

which we discretize by means of a conservative approximation:

$$\frac{\mathrm{d}v_i}{\mathrm{d}t} + a\frac{1}{h}\left(\tilde{v}_{i+1/2} - \tilde{v}_{i-1/2}\right) = 0. \tag{12}$$

A particular solution of (11) is given by a monochromatic wave of wavenumber k,

$$v(x,t) = e^{\mathrm{i}k(x-at)},$$

which on a uniform grid becomes

$$v_i(t) = e^{\mathrm{i}\hat{k}(i-a/ht)}, \tag{13}$$

where $\hat{k} = kh$ is the *scaled wavenumber* [28], which is directly related to the number of grid points per wavelength (n_p)

$$\hat{k} = \frac{2\pi}{n_p}; \tag{14}$$

note that the highest resolvable wavenumber corresponds to $n_p = 2$, which implies that it is sufficient for the sake of the analysis to consider the range of scaled wavenumbers $0 \le \hat{k} \le \pi$. If the semidiscretization (5) + (12) is used instead of the exact solution, one obtains

$$\begin{aligned} v_i(t) &= e^{\mathrm{i}\hat{k}(i-\frac{a}{h}\frac{z(\hat{k})}{\hat{k}}t)} \\ &= e^{\frac{a}{h}\mathrm{Im}[Z(\hat{k})]t}\, e^{\mathrm{i}\hat{k}(i-\frac{a}{h}\frac{\mathrm{Re}[Z(\hat{k})]}{\hat{k}}t)}, \end{aligned} \tag{15}$$

where

$$Z(\hat{k}) = 2\sin\hat{k}/2\frac{\sum_{m=-M_1}^{M_2} a_m e^{\mathrm{i}\hat{k}m}}{\sum_{l=-L_1}^{L_2} \alpha_l e^{\mathrm{i}\hat{k}(l+1/2)}}. \tag{16}$$

The *transfer function* $Z(\hat{k})$ therefore completely describes the behavior of the numerical scheme for sinusoidal initial conditions of a given scaled wavenumber $\hat{k}$. It is also evident, from a comparison with the exact solution, which propagates at a phase speed a and does not decay with time, that the discrete approximation causes a dispersion error, as the numerical approximation propagates at the phase speed $a\mathrm{Re}(Z)/\hat{k}$, where $Z(\hat{k})$ is generally different from $\hat{k}$, and damps out with time at a rate $e^{a/h\mathrm{Im}[Z(\hat{k})]t}$. It is therefore necessary for the stability of the semidiscrete algorithm that $\mathrm{Im}[Z(\hat{k})] \le 0$ (of course the opposite holds for left-running waves, for which $a < 0$ and therefore for stability one must have $\mathrm{Im}[Z(\hat{k})] \ge 0$).

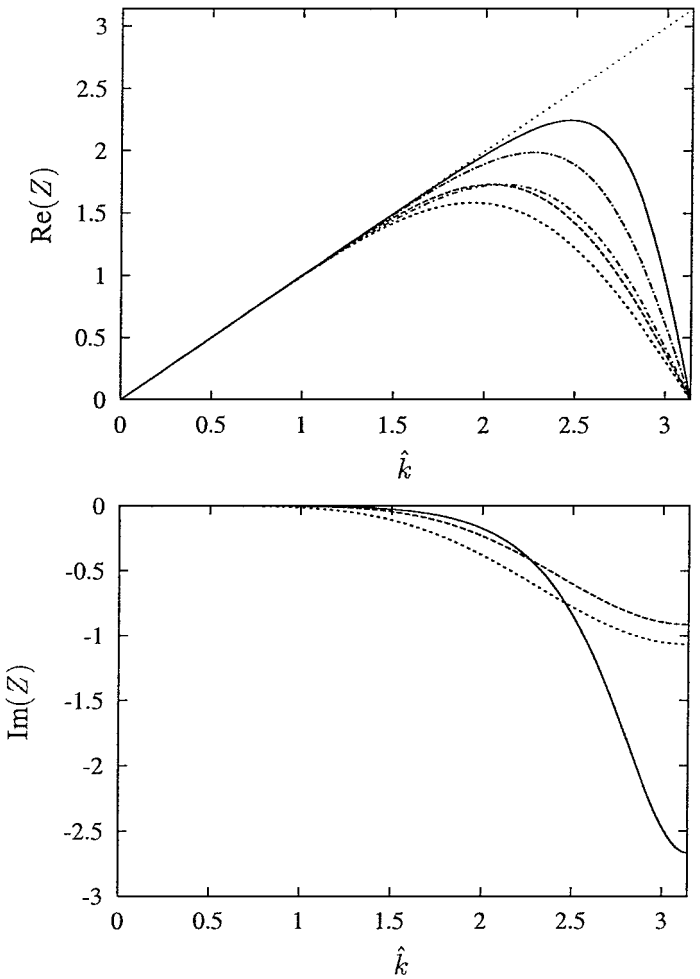

FIG. 1. Dispersion and dissipation properties for different approximation schemes. ——, Fifth-order compact upwind scheme; – – –, seventh-order WENO; - - -, fifth-order WENO; – · – · –, sixth-order Padé; - · - · -, fourth-order Padé; · · · ·, spectral ($Z(\hat{k}) = \hat{k}$).

The transfer function for the fifth-order compact upwind algorithm here proposed (Eq. 8) is plotted in Fig. 1, together with the transfer function associated with the explicit fifth- and seventh-order upwind schemes (Eqs. (9) and (10)). In the same figure we also report the transfer functions associated with the classical fourth-order, three-point-stencil Padé scheme and for the sixth-order, five-point-stencil compact algorithm reported by Lele [9, 28], which are given respectively by

$$Z_{\text{Padé-4}}(\hat{k}) = \frac{3\sin\hat{k}}{2+\cos\hat{k}},$$

$$Z_{\text{Padé-6}}(\hat{k}) = \frac{28\sin\hat{k}+\sin(2\hat{k})}{18+12\cos\hat{k}},$$

For reference purposes we also report the transfer function of a spectral scheme, which is simply $Z(\hat{k}) = \hat{k}$. The figure shows that the proposed scheme yields much better resolution

properties than the explicit weighted ENO schemes, and than the Padé schemes as well, and propagates at the correct speed waves with $\hat{k} \leq 2$ (i.e., is able to capture sinusoidal waves with three points per wavelegth). Figure 1 also shows that the dissipation error is confined to high wavenumbers, where the compact upwind scheme exhibits a larger dissipation than the other ones. This is not necessarily a bad feature, as in the range of high wavenumbers the waves propagate at an incorrect speed, and it can be desirable to damp them as much as possible. This feature is also desirable for Euler flow calculations, where the molecular viscosity is zero, and some numerical viscosity is often necessary to prevent aliasing errors from growing without bound.

In the present work no optimization of the compact scheme in the wavenumber space has been attempted, as done in Refs. [1, 14, 42, 49], among the others. However, it has been found that the selected fifth-order compact scheme is nearly optimal for its resolution properties among the family of compact schemes here developed. Finally, we observe that the propagation characteristics of the scheme here proposed are intermediate between the two compact schemes proposed by Adams and Shariff [1] (which those authors refer to as CUHD, which stands for compact upwind high dissipation, and CULD, low dissipation); in particular the dispersion characteristics of the proposed scheme are closer to CULD, while the diffusion characteristics are closer to CUHD. However, those schemes require the inversion of a pentadiagonal matrix rather than a tridiagonal one.

2.2. Boundary Closures

The formulation of appropriate boundary closures is crucial for the formulation of a compact scheme that works properly [28], mostly because of the global nature of the reconstruction step, which involves all the nodes at a time. Indeed, boundary closures critically impact the stability characteristics of the scheme, and a stability study based on the decomposition into Fourier harmonics may lead to wrong conclusions. Rather, a stability analysis of the full discretization becomes necessary. We propose the following (fourth order) explicit boundary closures for the left and right boundary, respectively:

$$\begin{aligned} \tilde{v}_{1/2} &= \frac{1}{4}v_0 + \frac{13}{12}v_1 - \frac{5}{12}v_2 + \frac{1}{12}v_3, \\ \tilde{v}_{N+1/2} &= \frac{25}{12}v_N - \frac{23}{12}v_{N-1} + \frac{13}{12}v_{N-2} - \frac{1}{4}v_{N-3}. \end{aligned} \tag{17}$$

It has been shown [18] that this is sufficient to maintain fifth-order accuracy for the global discretization. Note that the latter boundary closures are consistent with the physical nature of the problem under investigation (Eq. (11)), which corresponds to the propagation of right-running disturbances. Indeed, the value of $\tilde{v}$ at the right boundary (i.e., the intermediate node $x_{N+1/2}$) is extrapolated from the interior, whereas the evaluation of the numerical flux at the left boundary at the intermediate node $x_{1/2}$ requires the knowledge of the solution in an additional *ghost* node x_0, which serves to enforce a physical boundary condition related to the amplitude of an incoming disturbance.

For the purpose of determining the stability characteristics of the compact upwind scheme here developed (Eq. (8)), supplemented with the boundary closures (17), let us introduce a compact matrix notation. First, the reconstruction stage is implicitly described by

$$\mathbf{A}\tilde{\mathbf{v}} = \mathbf{B}\mathbf{v} + \mathbf{b}, \tag{18}$$

where $\mathbf{v} = (v_1, v_2, \ldots, v_N)^T$, $\tilde{\mathbf{v}} = (\tilde{v}_{1/2}, \tilde{v}_{3/2}, \ldots, \tilde{v}_{N+1/2})^T$, $\mathbf{b} = (1/4 v_0, 0, \ldots, 0)^T$, and

$$\mathbf{A} = \begin{bmatrix} 1 & & & & & & \\ 3 & 6 & 1 & & & & \\ & 3 & 6 & 1 & & & \\ & & \ddots & \ddots & \ddots & & \\ & & & 3 & 6 & 1 & \\ & & & & & 1 & \end{bmatrix}, \quad \mathbf{B} = \begin{bmatrix} \frac{13}{12} & -\frac{5}{12} & \frac{1}{12} & & & & \\ \frac{19}{3} & \frac{10}{3} & & & & & \\ \frac{1}{3} & \frac{19}{3} & \frac{10}{3} & & & & \\ & \ddots & \ddots & \ddots & & & \\ & & \frac{1}{3} & \frac{19}{3} & \frac{10}{3} & & \\ & & -\frac{1}{4} & \frac{13}{12} & -\frac{23}{12} & \frac{25}{12} & \end{bmatrix}. \tag{19}$$

Second, the conservative approximation for the first derivative is written as

$$\mathbf{v}' = \frac{1}{h}\mathbf{C}\tilde{\mathbf{v}}, \tag{20}$$

with

$$\mathbf{C} = \begin{bmatrix} -1 & 1 & & \\ & \ddots & \ddots & \\ & & -1 & 1 \end{bmatrix}. \tag{21}$$

The following semidiscrete approximation to (11) therefore holds

$$\mathbf{v}_t = -\frac{a}{h}\mathbf{C}\mathbf{A}^{-1}(\mathbf{B}\mathbf{v} + \mathbf{b}). \tag{22}$$

It is then clear that the stability characteristics of the semidiscrete approximation depend upon the matrix $\mathbf{S} = -\mathbf{C}\mathbf{A}^{-1}\mathbf{B}$. In particular, a necessary condition for stability is that all eigenvalues of $\mathbf{S}$ have negative real part and therefore correspond to exponentially damped modes. In order to analyze the stability properties of the scheme (12) + (8) + (17) we then have numerically computed the eigenvalues of the matrix $\mathbf{S}$ for several values of the number of grid points. The results of the analysis are reported in Fig. 2, where we also report the

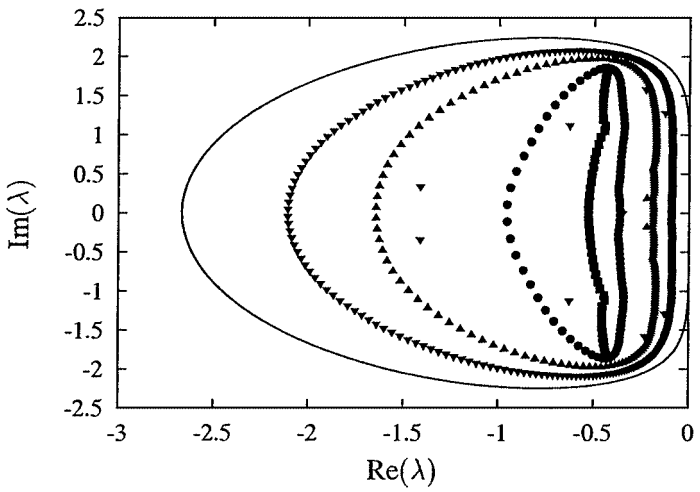

FIG. 2. Eigenvalue spectra for the compact upwind scheme. ■, $N = 50$; ●, $N = 100$; ▲, $N = 200$; ▼, $N = 400$; ——, periodic.

spectrum of **S** for the case of periodic boundary conditions. In the latter case the matrix **S** is circulant, and as such its eigenvalues are given by [45]

$$\lambda_m = -\mathbf{i}Z(2\pi m/N), \quad m = 1, \ldots, N, \tag{23}$$

with Z given in Eq. (16). The figure clearly shows that the selected scheme supplemented with appropriate boundary conditions is linearly stable regardless of the number of grid points. In addition, the figure also shows that the effect of the boundary closures (17) is to stabilize the overall algorithm; indeed, the eigenvalue spectrum in the presence of boundary closures entirely lies inside the region bounded by the eigenvalue spectrum for periodic boundary conditions.

2.3. Stability Analysis of the Full Discretization

In the present work we have employed a method of lines approach, whereby the time integration is performed by means of a four-stage, fourth-order, non-TVD Runge–Kutta scheme. For a system of ODEs

$$\frac{\mathrm{d}\mathbf{v}}{\mathrm{d}t} = \mathcal{L}(\mathbf{v}), \tag{24}$$

the chosen scheme can be written as

$$\begin{aligned}
\mathbf{v}^{(1)} &= \mathbf{v}^n + \frac{1}{2}\Delta t\,\mathcal{L}(\mathbf{v}^n),\\
\mathbf{v}^{(2)} &= \mathbf{v}^n + \frac{1}{2}\Delta t\,\mathcal{L}\big(\mathbf{v}^{(1)}\big),\\
\mathbf{v}^{(3)} &= \mathbf{v}^n + \Delta t\,\mathcal{L}\big(\mathbf{v}^{(2)}\big),\\
\mathbf{v}^{n+1} &= \frac{1}{3}\big(-\mathbf{v}^n + \mathbf{v}^{(1)} + 2\mathbf{v}^{(2)} + \mathbf{v}^{(3)}\big) + \frac{1}{6}\Delta t\,\mathcal{L}\big(\mathbf{v}^{(3)}\big).
\end{aligned} \tag{25}$$

The operator $\mathcal{L}$ that appears at the right-hand side of Eq. (24) stems from the discretization of the spatial part of a conservation equation; for example, in the case of Eq. (11) (whose semidiscretized form is given by Eq. (22)) we can identify $\mathcal{L} \equiv a/h\mathbf{S}$, disredarding the forcing term. The stability analysis for the full discretization of Eq. (11) has been here carried out exploiting a von Neumann normal mode analysis. Note that such an analysis is in general not strictly justifyable for the case of nonperiodic boundary conditions, and one has to revert to more general methods of stability analysis, such as the matrix method [21]. However, we observe that when the boundary conditions provide a damping for the spatial discretization operator, a von Neumann analysis is sufficient in practice. It turns out [45] that for the fourth-order Runge–Kutta time integration scheme the amplitude $\hat{v}(\hat{k})$ of a generic Fourier mode whose scaled wavenumber is $\hat{k}$ at the time step $n+1$ is related to its amplitude at time step n through the relation

$$\hat{v}^{n+1}(\hat{k}) = g(\hat{k})\hat{v}^n(\hat{k}), \tag{26}$$

where $g(\hat{k})$ is called the *amplification factor* for the fully discrete algorithm, given by

$$g(\hat{k}) = \left[1 + \mathrm{i}\sigma Z + \frac{1}{2}(\mathrm{i}\sigma Z)^2 + \frac{1}{6}(\mathrm{i}\sigma Z)^3 + \frac{1}{24}(\mathrm{i}\sigma Z)^4\right], \tag{27}$$

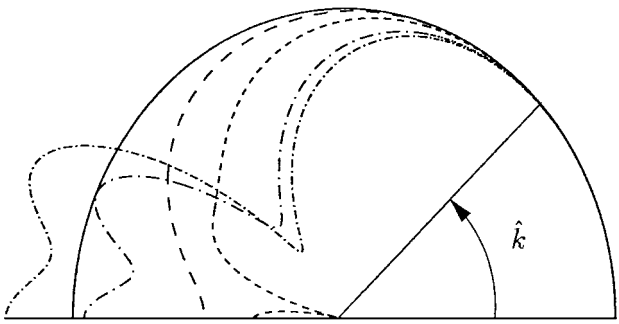

FIG. 3. Amplification factor of the fully discrete scheme as a function of the scaled wavenumber $\hat{k}$. ——, Unit circle; – – –, $\sigma = 0.25$; - - -, $\sigma = 0.75$; – · – · –, $\sigma = 1.034$; · · · · ·, $\sigma = 1.1$.

where $\sigma = a\Delta t/h$ is the Courant number, and $Z(\hat{k})$ is the transfer function associated with the spatial discretization operator. The full discretization will therefore prove to be von Neumann stable provided the condition $|g(\hat{k})| \leq 1$ is satisfied for $|\hat{k}| \leq \pi$. In Fig. 3 we report in a polar plot the distribution of $|g(\hat{k})|$ for several values of σ (note that only the range $0 \leq \hat{k} \leq \pi$ is plotted in the figure because $|g|$ is an even function of $\hat{k}$). The figure shows that the stability condition is

$$\sigma \leq 1.034. \tag{28}$$

It is interesting to observe that the price to pay to have better resolution properties is to have a more limited range of stability with respect to the linear WENO schemes reported in Eqs. (9) and (10) in their fifth-order ($W5$) and the seventh-order ($W7$) version. Indeed, the von Neumann stability analysis of those schemes results in the following stability ranges:

$$\sigma_{W5} \leq 1.732, \quad \sigma_{W7} \leq 1.689. \tag{29}$$

2.4. A Convergence Test on Smooth Solutions

In order to numerically test the convergence of the compact scheme here developed we have performed a series of preliminary simulations whereby we have considered the solution of the linear advection Eq. (11) with smooth initial conditions and with unit advection speed ($a = 1$). In particular, we have considered a computational domain $-1 \leq x \leq 1$ with the following initial conditions: (a) $v(x, 0) = \sin(\pi x)$; (b) $v(x, 0) = \sin^4(\pi x)$. A uniformly spaced grid has been used with a time step which is varied with the number of grid points according to $\sigma \propto N^{-1/4}$ so as to rule out the time discretization error. The computed results have been compared to the exact solution at time $t = 2$. The results of the study are reported in Fig. 4. In the figure we report the distribution of the L_1, L_2, and L_∞ errors as a function of the number of grid points. For reference purposes, we also report dashed lines with an N^{-5} slope, which is consistent with the formal order of accuracy of the scheme. The figure shows that the asymptotic convergence rate is achieved for both test cases even on coarse grids.

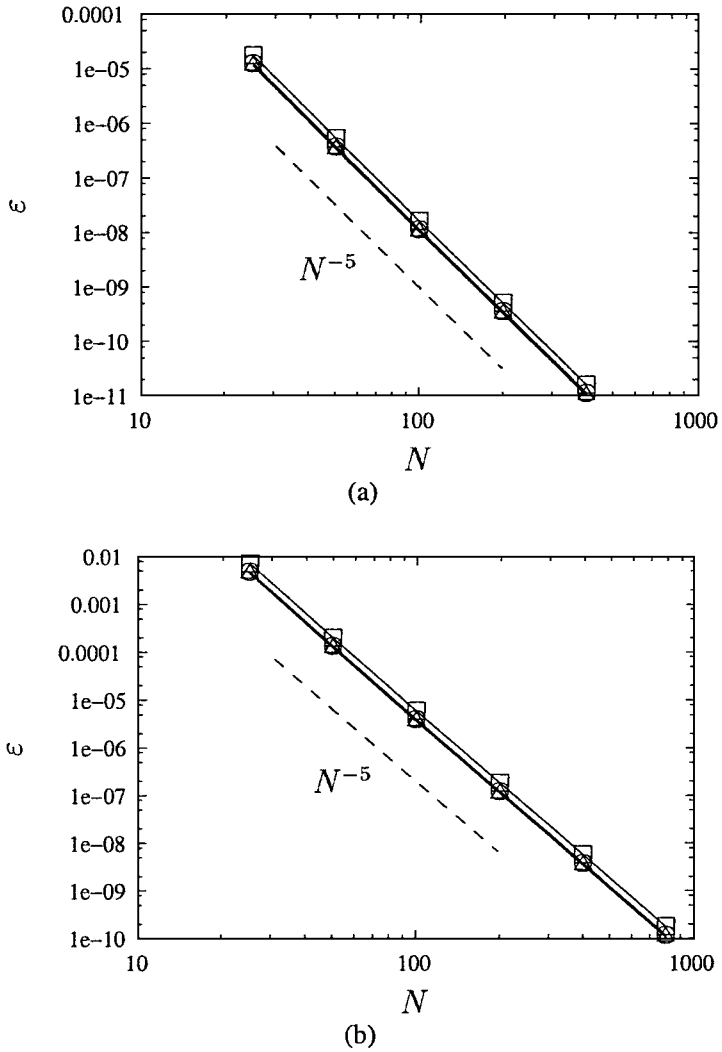

FIG. 4. Convergence study for smooth initial conditions. (a) $v(x, 0) = \sin(\pi x)$; (b) $v(x, 0) = \sin^4(\pi x)$. □, L_∞ error, ○, L_2 error; △, L_1 error.

3. COUPLING WITH WEIGHTED ENO SCHEMES

The compact upwind scheme described in the previous section has been demonstrated to converge for smooth solutions provided appropriate boundary closures are given. However, in the presence of discontinous solutions Gibbs phenomena do occur, which contaminate the solution and may lead to nonlinear instability. In order to cure this deficiency, linear algorithms must be replaced with nonlinear ones, which have a shock-capturing capability. Good examples of such schemes are the so-called total variation diminishing (TVD) schemes, the essentially nonoscillatory (ENO) schemes, and the more recent weighted essentially nonoscillatory (WENO) schemes, which probably represent the best compromise between accuracy and computational cost. We now briefly discuss the basics of the WENO schemes, following the formulation of Jiang and Shu [22] and Shu [39].

The basic idea of the WENO interpolation is to introduce a convex linear combination of low-order polynomial reconstructions that yield a higher order reconstruction in smooth regions, and with weights chosen so as to favor the reconstruction over smooth stencils rather than over irregular ones. In the WENO approach the the numerical flux can be expressed as

$$\tilde{v}_{i+1/2} = \sum_{r=0}^{k-1} \omega_r \tilde{v}^{(r)}_{i+1/2}, \tag{30}$$

where the low-order polynomial reconstructions $\tilde{v}^{(r)}$ are obtained as linear combinations of the point values of function v according to

$$\tilde{v}^{(r)}_{i+1/2} = \sum_{l=0}^{k-1} c^{(r)}_l v_{i-r+l},$$

and the constants $c^{(r)}_l$ are determined from a linear interpolation problem, as discussed in Section 2. The weights ω_r satisfy the conditions

$$\omega_r \geq 0, \quad \sum_{r=0}^{k-1} \omega_r = 1$$

and are designed to yield $(2k-1)$th-order accuracy in the absence of discontinuities, and to select the smoothest stencil over the other ones. This implies a lower order of accuracy in the vicinity of shock waves but at the same time prevents the occurrence of Gibbs phenomena. In particular, Refs. [22, 39] use

$$\omega_r = \frac{d_r/(\epsilon + \beta_r)^2}{\sum_{l=0}^{k-1} d_l/(\epsilon + \beta_l)^2}, \tag{31}$$

where d_r is the *ideal* weight, β_r is a smoothness indicator for the rth stencil, and ϵ is a small parameter, necessary to avoid divisions by zero. It is possible to show that the ideal weights d_r can be constructed so that a linear combination of k polynomial reconstructions of kth order yield a $(2k-1)$th-order overall reconstruction. A proper definition of the smoothness indicators is crucial for the scheme to perform correctly; we have employed the smoothness indicators proposed in Ref. [22], i.e.,

$$\beta_r = \sum_{l=1}^{k-1} h^{2l+1} \int_{x_{i-1/2}}^{x_{i+1/2}} \left[\frac{\partial^l v^{(r)}}{\partial \xi^l} \right]^2 \mathrm{d}\xi. \tag{32}$$

Numerical values for the coefficients $c^{(r)}_l$ and d_r and for the smoothness sensors β_r are provided for $k = 2, 3$ in Ref. [39], while the data for schemes of higher order (from the seventh on) are reported in Ref. [4]. It is interesting to observe that the fifth- and the seventh-order WENO schemes reduce to the linear upwind schemes (9) and (10), respectively, in smooth regions.

In the framework of a fully conservative formulation it is a simple task to interface the compact upwind algorithm with the WENO one, turning it on in nonsmooth regions. The simplest criterion that can be devised, and that has been successfully used by other authors [1, 31], is based on the evaluation of the absolute value of the difference of the computed solution in the two adjacent nodes, i.e.,

$$|v_{i+1} - v_i|. \tag{33}$$

When the difference is larger than a threshold value β, the flux function at the intermediate node $i + 1/2$ and the two neighboring ones ($i - 1/2$ and $i + 3/2$) is computed by means of the WENO algorithm. Therefore, only the reconstruction stage is affected. More elaborate switches to locally apply numerical dissipation have recently been proposed in the literature [16, 50]. These approaches have not been investigated in the present paper and are the subject on ongoing research. To show how this procedure can work, let us refer to a situation where the function v to interpolate has a single point of discontinuity between the nodes i and $i + 1$, whereas it is sufficiently smooth on both sides of the discontinuity. For example, let us consider the case $k = 3$, which yields a fifth-order WENO scheme. It is then easy to show that the matrices involved in the interpolation (Eq. (18)) are changed as follows:

$$\mathbf{A} = \left[\begin{array}{ccccc|ccccc} 1 & & & & & & & & & \\ 3 & 6 & 1 & & & & & & & \\ & \ddots & \ddots & \ddots & & & & & & \\ & & & 1 & & & & & & \\ & & & & 1 & & & & & \\ \hline & & & & & 1 & & & & \\ & & & & & 3 & 6 & 1 & & \\ & & & & & & \ddots & \ddots & \ddots & \\ & & & & & & & & & 1 \end{array}\right],$$

$$\mathbf{B} = \left[\begin{array}{ccccc|ccccc} \frac{13}{12} & -\frac{5}{12} & \frac{1}{12} & & & & & & & \\ \frac{19}{3} & \frac{10}{3} & & & & & & & & \\ \frac{1}{3} & \frac{19}{3} & \frac{10}{3} & & & & & & & \\ & \ddots & \ddots & \ddots & & & & & & \\ & \frac{1}{21} & -\frac{13}{42} & \frac{41}{42} & \frac{2}{7} & & & & & \\ & & \frac{1}{3} & -\frac{7}{6} & \frac{11}{6} & & & & & \\ \hline & & & & & \frac{1}{3} & \frac{5}{6} & -\frac{1}{6} & & \\ & & & & & \frac{1}{3} & \frac{19}{3} & \frac{10}{3} & & \\ & & & & & & \ddots & \ddots & \ddots & \\ & & & & & -\frac{1}{4} & \frac{13}{12} & -\frac{23}{12} & \frac{25}{12} & \end{array}\right]. \tag{34}$$

Hence, the interpolated values in the nodes $(v_{1/2}, \ldots, v_{i+1/2})$ and $(v_{i+3/2}, \ldots, v_{N+1/2})$ are independent of each other, and interpolation across the discontinuity is avoided.

In the following, we analyze the performance of weighted ENO schemes of fifth- and seventh-order, which we refer to as $W5$ and $W7$, respectively. At the same time, we consider hybrid schemes constructed by coupling the basic fifth-order compact upwind algorithm described in Section 2 with the fifth- and seventh-order WENO schemes, and these are referred to as $H5$ and $H7$.

3.1. A Test on the Linear Advection Equation

In order to test the capability of the hybrid compact-WENO algorithm to compute discontinuous solutions, we carried out a preliminary study whereby we considered the linear

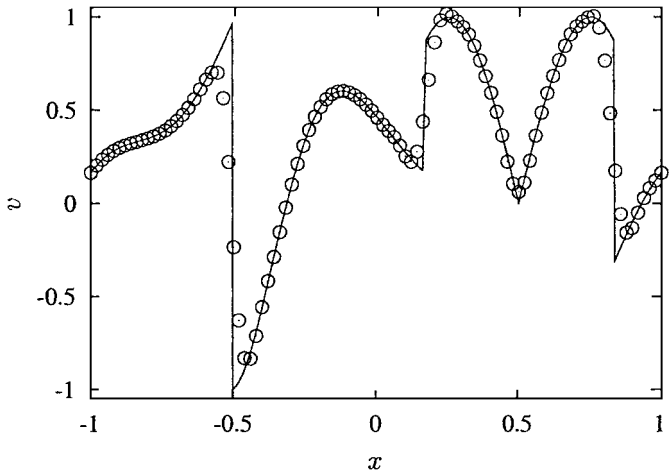

FIG. 5. Numerical solution of Harten's test case with the hybrid scheme $H7$ ($N = 100$, $\beta = 0.25$). ○, Computed solution; ——, exact solution.

advection equation (Eq. (11)) with the discontinuous initial conditions

$$v(x + 0.5, 0) = \begin{cases} -x \sin(3/2\pi x^2), & -1 \le x < -1/3, \\ |\sin(2\pi x)|, & |x| < 1/3, \\ 2x - 1 - \sin(3\pi x)/6, & 1/3 < x < 1, \end{cases} \tag{35}$$

and supplemented with periodic boundary conditions at $x = \pm 1$. This test case was originally proposed by Harten *et al*. [20], and then used by many authors as a simple test to check the capability of a numerical scheme to handle solutions with flow discontinuities and smooth regions at the same time. The solution has been computed using a Courant number $\sigma = 0.5$ and the solutions are reported at time $t = 2$, which corresponds to a distance of one wavelength. The solution obtained with the $H7$ scheme for $N = 100$ and $\beta = 0.25$ is reported in Fig. 5, together with the exact solution. From inspection of the figure one can clearly see that the numerical algorithm develops accurate solutions in the smooth regions and captures the discontinuities without observable oscillations, causing only a little smearing around the latter.

It is important to wonder how the computed solution depends upon the number of grid points, as well as on the numerical parameter β. For this purpose we have shown in Fig. 6 the distribution of the L_1 norm of the solution error as a function of the number of grid points and of β. The figure shows that the error monotonically decreases with the number of grid points, although at a rate that is slower than in the case of smooth solutions (see Fig. 4). Indeed, the convergence rate is reduced to N^{-1} approximately, which is to be expected when discontinuities are involved. In addition, the figure shows that the error is a monotonically decreasing function of β. One should then observe that $\beta = 0$ corresponds to the $W7$ scheme, while $\beta = 1$ (for the present test case) corresponds to using the linear compact upwind scheme (8) for all the nodes. However, as β is increased, the Gibbs phenomenon starts to show itself under the form of spurious oscillations around the discontinuities. Such oscillations are not particularly harmful in the case of the linear advection equation, but they may affect more seriously the solution in the case of the Euler equations, for example, in which case nonlinear instabilities are likely to occur. Therefore, although the global error

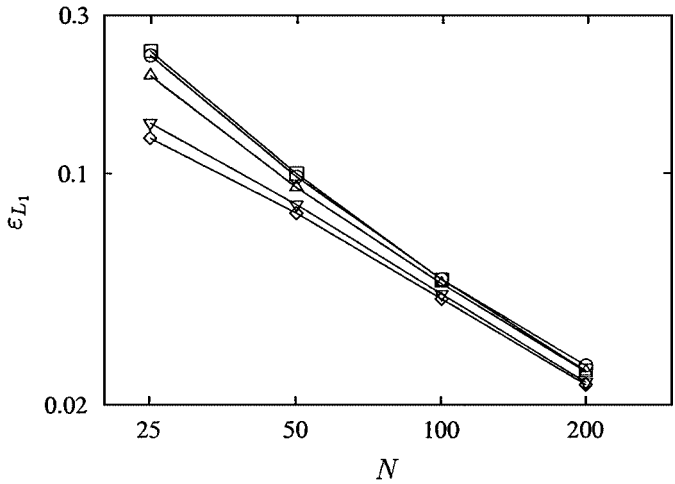

FIG. 6. Convergence study for Harten's test case. □, $\beta = 0$; ○, $\beta = 0.1$; △, $\beta = 0.25$; ▽, $\beta = 0.5$; ◇, $\beta = 1$.

decreases by allowing the scheme to bias toward a compact scheme, when dealing with nonlinear systems of equations, one is left with the problem of balancing the accuracy requirements with the necessity of keeping the computation stable. The choice of a proper value for β is further discussed in the following.

4. EXTENSION TO THE EULER EQUATIONS OF GAS DYNAMICS

The main focus of the present work is in solving the Euler equations of gas dynamics, which are written in conservation form as

$$\frac{\partial \mathbf{v}}{\partial t} + \sum_{j=1}^{d} \mathbf{f}_j(\mathbf{v})_{x_j} = 0, \tag{36}$$

where $\mathbf{v}$ is the vector of conservative variables, $\mathbf{f}_j$ is the flux vector in the jth coordinate direction, and d is the space dimension of the problem. The procedure here developed relies on a local characteristic decomposition of the governing equations that exploits the hyperbolic character of the Euler system. The Jacobians of the flux vectors are similar to diagonal matrices, according to

$$\frac{\partial \mathbf{f}_j}{\partial \mathbf{v}} = \mathbf{R}_j \mathbf{\Lambda}_j \mathbf{L}_j,$$

where $\mathbf{\Lambda}_j$ is the matrix of the characteristic velocities in the jth direction, and $\mathbf{R}_j$ and $\mathbf{L}_j$ are the matrices of the right and left eigenvectors, respectively. Upwinding is achieved by splitting $\mathbf{\Lambda}_j$ into positive and negative parts, i.e.,

$$\mathbf{\Lambda}_j = \mathbf{\Lambda}_j^+ + \mathbf{\Lambda}_j^-. \tag{37}$$

This can be done in several ways [21], and for example one can write

$$(\lambda_l^{\pm})_j = \frac{1}{2}[(\lambda_l)_j \pm (\lambda_l^*)_j],$$

where

$$(\lambda_l^*)_j = \max_{x_j} |(\lambda_l)_j|,$$

and the maximum is taken over the relevant range of x_j involved in the reconstruction. In the present case, since the reconstructions are inherently global, the maximum is taken over the entire range $x_1 \leq x_j \leq x_{N_j}$. Exploiting the homogeneity property of the Euler equations, the splitting (37) induces the (Lax–Friedrichs) flux splitting

$$\mathbf{f}_j^{\pm} = \frac{1}{2}(\mathbf{f}_j \pm \mathbf{R}_j \mathbf{\Lambda}_j^* \mathbf{L}_j \mathbf{v}), \tag{38}$$

which has the obvious property $\mathbf{f}_j = \mathbf{f}_j^+ + \mathbf{f}_j^-$. The positive part of the split fluxes $\mathbf{f}_j^+$ (which are associated with positive propagation velocities) are then discretized according to the scalar upwind methodology described in the previous sections component by component, whereas the negative split fluxes are discretized by means of the analogous upwind formulae that can be obtained for waves with negative propagation velocities according to trivial symmetry consideration. A cheaper, even though more dissipative, Lax–Friedrichs flux splitting is obtained by considering the maximum of the characteristic velocities over all the characteristic fields,

$$(\lambda_l^{\pm})_j = \frac{1}{2}[(\lambda_l)_j \pm \alpha_j],$$

where

$$\alpha_j = \max_l (\lambda_l^*)_j.$$

The flux splitting then obtained is

$$\mathbf{f}_j^{\pm} = \frac{1}{2}(\mathbf{f}_j \pm \alpha \mathbf{v}), \tag{39}$$

whereby the evaluation of the eigenvector matrices is avoided. In the following we refer to the first type of splitting as the low-dissipation Lax–Friedrichs (LDLF), while the second one is referred to as the high-dissipation Lax–Friedrichs (HDLF).

It is important to point out that for systems of conservation equations there are several alternatives for defining the smoothness measurement needed to couple the compact and the WENO algorithms (Eq. (33)). A simple choice is to evaluate the smoothness properties on the basis of the density field only and apply the WENO algorithm selectively in the regions of the flow field where

$$|\rho_{i+1} - \rho_i| > \beta. \tag{40}$$

This choice guarantees that both shock waves and contact discontinuities are properly recognized. Also, several choices are available for computing the smoothness estimators β_r needed to compute the nonlinear weights involved with the WENO algorithm. Consistently, we have chosen to use smoothness estimators based on the density only, which also allow a consistent saving in terms of computation times.

5. APPLICATIONS

In the present section we discuss the application of the hybrid algorithm here developed for some test cases that have been extensively studied in the literature. In addition, we also report the results obtained from the simulation of a three-dimensional shock-turbulence interaction problem. Note that for all the applications, unless otherwise specified, the LDLF flux splitting of Eq. (38) has been used.

5.1. Inviscid Burgers Equation

To test the efficiency of the schemes discussed in the previous sections on nonlinear problems with discontinuous solutions, we have considered the one-dimensional inviscid Burgers equation,

$$v_t + \left(\frac{v^2}{2}\right)_x = 0, \tag{41}$$

which has been solved in the domain $-1 \le x \le 1$ with the (smooth) initial conditions

$$v(x, 0) = 0.3 + 0.7 \sin \pi(x + 1),$$

and with periodic boundary conditions. The solution to the problem consists of a steepening wave propagating to the right, which gives rise to a shock wave at a time $t^* = 1/(0.7\pi)$. The numerical solution has been obtained by considering a uniformly spaced grid with N grid points and a constant time step with $\sigma = 0.5$. The flux splitting has been performed according to

$$f^{\pm} = \frac{1}{2}\left(\frac{v^2}{2} \pm \alpha v\right),$$

where $\alpha = \max_{i=1,N} |v_i|$. The parameter β which controls the switch between the compact and the WENO scheme has been set to $\beta = 0.1$, so as to be compared more precisely with the results obtained by Adams and Shariff [1]. The computations have been time advanced up to a time $t = 2/\pi$, when a shock wave has already formed. The computed results with various algorithms and for $N = 20$ are reported in Fig. 7, together with the analytical solution. The figure gives evidence of the capability of the four schemes to correctly compute the discontinous solution without (observable) oscillations. However, the figure shows some differences in the computed solutions close to the shock, where the schemes $W7$ and $H7$, which both rely on the seventh-order WENO scheme around the discontinuity, provide a somewhat less smeared solution with respect to the $W5$ and $H5$ algorithms. In order to better appreciate the difference between the various schemes, in Fig. 8 we report the distribution of the pointwise error for $N = 80$. The figure confirms that the behavior of the local error in the proximity of the shock wave is dominated by the order of the WENO algorithm. Far from the shock, small oscillations are discernible. The error is larger for the $W5$ scheme upstream of the shock than for the $W7$ scheme, whereas the opposite holds downstream of the shock. The hybrid schemes $H5$ and $H7$ exhibit a similar behavior far from the shock and apparently do not suffer from spurious oscillation generated at the interface between the compact and the shock-capturing scheme, as observed in Ref. [1] for the CULD scheme.

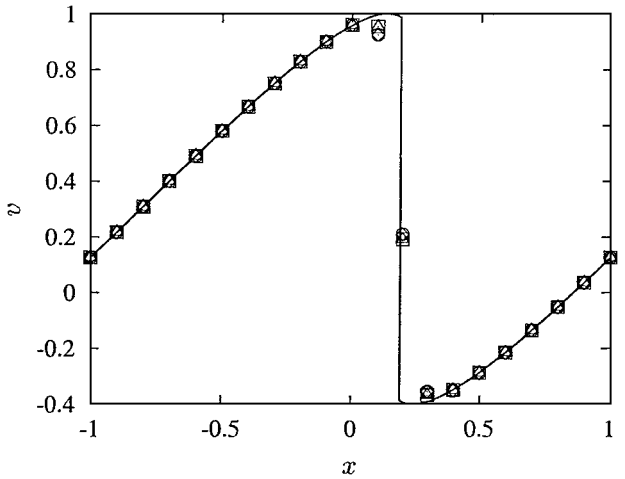

FIG. 7. Numerical solution of Burgers equation at $t = 2/\pi (N = 20)$. ——, Exact solution; □, $H7$; ○, $H5$; △, $W7$; ◇, $W5$.

As a final check of the capabilities of the hybrid schemes, in Fig. 9 we report the variation of the L_1 norm error of the computed solution, as a function of the number of grid points. As is done in Ref. [1], the error is computed considering only the points lying away from the shock, i.e., excluding the region $x_{sh} - 0.1 < x < x_{sh} + 0.1$. Figure 9 shows that the error on coarse grids is dominated by the treatment of the shock, and indeed the schemes $W5$ and $H5$, $W7$ and $H7$ behave in a similar manner. However, on very fine meshes ($N \geq 320$), the error turns out to be mostly affected by the type of scheme employed in the smooth regions, and indeed the hybrid schemes $H5$ and $H7$ exhibit the same error level, which is a factor $2 \div 3$ lower than for the WENO schemes, and an overall N^{-5} scaling of the error.

5.2. Shock-Entropy Wave Interaction in 1D

The following test case is taken from Ref. [41] and has been studied by several other authors (see, e.g., Refs. [1, 19]). The one-dimensional Euler equation are solved with the

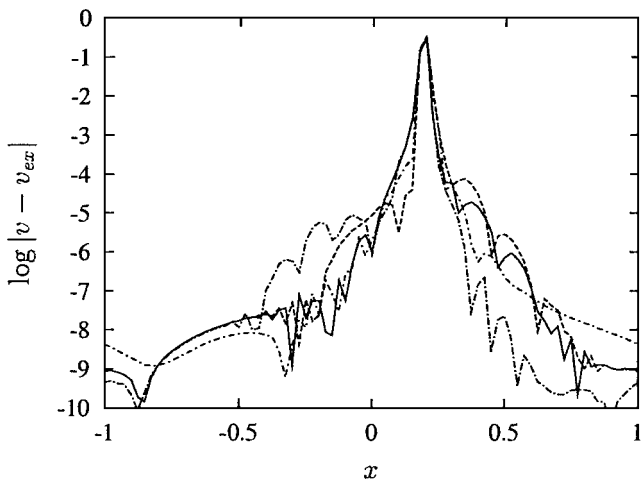

FIG. 8. Pointwise error for Burgers equation at $t = 2/\pi (N = 80)$. ——, $H7$; - - -, $H5$; – · – · –, $W7$; · · · · ·, $W5$.

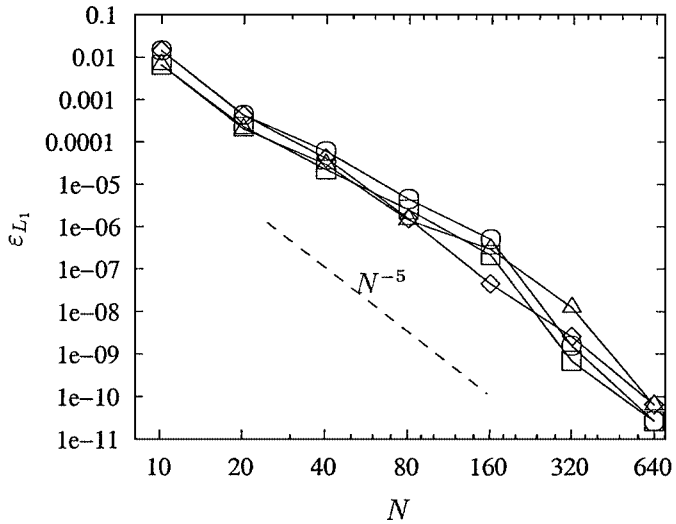

FIG. 9. Convergence study for Burgers equation. □, $H7$; ○, $H5$; △, $W7$; ◇, $W5$.

initial conditions

$$\mathbf{v}(x,0) = \begin{cases} \mathbf{v}_L, & x < -4, \\ \mathbf{v}_R, & x \geq -4, \end{cases}$$

where the initial left and right states are defined by the relations

$$\mathbf{v}_L = (\rho_L, u_L, p_L) = (3.857143, 2.629369, 10.333333),$$
$$\mathbf{v}_R = (\rho_R, u_R, p_R) = (1 + 0.2\sin(5x), 0, 1),$$

which reproduces the unsteady interaction of a $M = 3$ shock wave with a sine entropy wave that carries a density fluctuation of amplitude $\Delta\rho = 0.2$. An analytical solution is available in the literature for $\Delta\rho \ll 1$ [6, 32].

The numerical solution has been calculated in the interval $x \in [-5 : 5]$, and integrated forward in time up to $t = 1.8$. Zero time variation of the conservative variables has been specified at the left and right boundaries, which is appropriate for the time interval under interest. The time step has been set to a constant value

$$\Delta t = \sigma \frac{h}{\max_{i=1,N}(|u_i| + c_i)},$$

with a Courant number $\sigma = 0.5$. The switch parameter has been set to $\beta = 0.8$. This test case is particularly severe because the solution includes smooth regions with a rich structure consisting of receding acoustic waves (that steepen and give rise to shocklets) as well as entropy waves propagating downstream of the shock. The computed density fields for $N = 200$ are reported in Fig. 10, which is a rather marginal resolution. In the figure we also report the "exact" solution which we have obtained by computing the same problem with $N = 1600$. The figure demonstrates the superiority of the hybrid algorithms over the WENO ones in reproducing the correct flow features downstream of the shock. In particular, the $W5$ algorithm exhibits a serious damping of the entropy waves, while the $W7$ algorithm

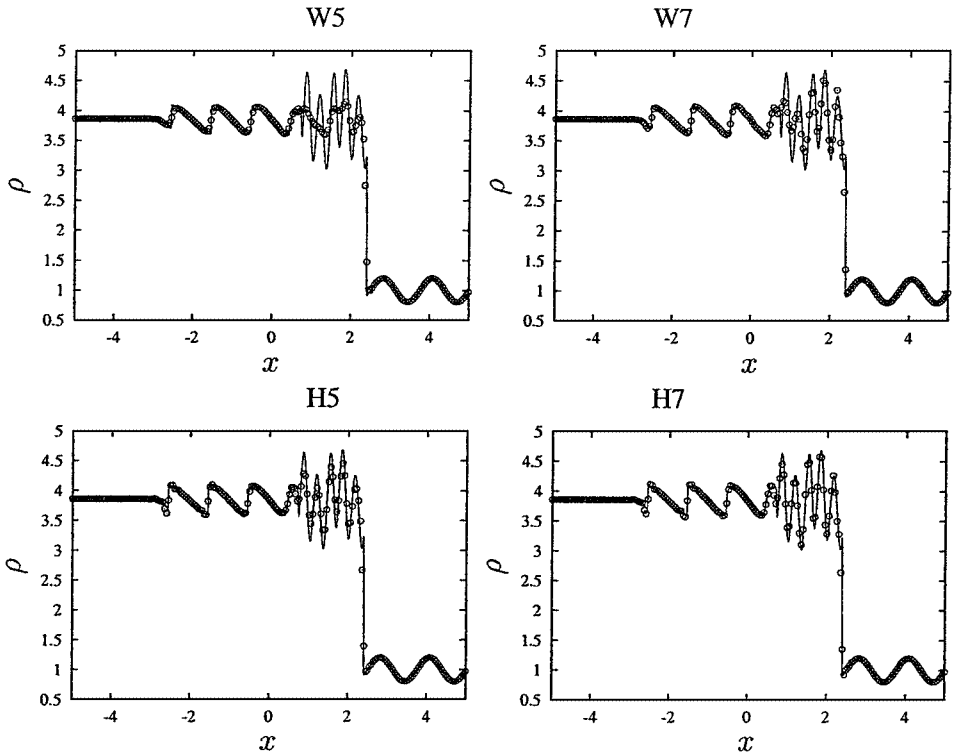

FIG. 10. Shock/entropy wave interaction: distribution of density for $N = 200(\beta = 0.8)$. ○, Computed solution; ——, "exact" solution.

shows poor results in the proximity of the interface between the acoustic and the entropy waves. The $H7$ scheme produces the best results among the algorithms here discussed, and in particular the amplitude of the entropy waves is predicted remarkably well. However, we also note that the hybrid algorithms produce some oscillations in the proximity of the shocklets, due to the relatively high value of β that has been chosen, such that the WENO apparatus is not turned on there. It is important to point out that the accuracy of the shock-capturing algorithm that is employed to treat discontinuities is of crucial importance for a good performance of the hybrid algorithm. Indeed, the $H7$ algorithm performs better than $H5$. At the same time, however, the use of a compact scheme away from the discontinuities is also observed to be beneficial, and indeed the $H5$ algorithm does better than the $W5$ and $H7$ does better than $W7$.

A comparison with the results reported by other authors [1, 19, 41] shows that the present hybrid formulation is capable of providing more accurate results, at least on coarse grids. In particular, a comparison with the results of Ref. [1] indicates that the present method provides better resolution properties downstream of the shock, even though the hybrid algorithm developed by those authors involves a pentadiagonal matrix inversion, rather than a tridiagonal one. The reason might be the use of a WENO reconstruction across discontinuous regions rather than a ENO one, but also the use of a fully conservative formulation may play an important role in obtaining better resolution properties.

The L_1 norm of the overall error (computed for $-5 \le x \le 2.25$, so that the shock is not included) is reported in Fig. 11. The figure indicates that on coarse grids (i.e., $N \approx 200$) the $H7$ algorithm has a lower error than the other ones, which is consistent with its better

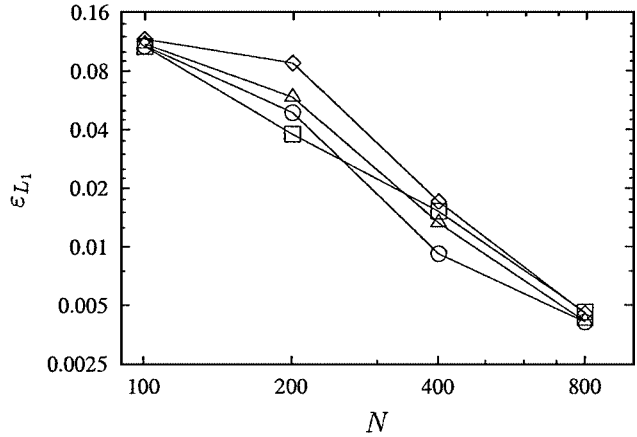

FIG. 11. Shock/entropy wave interaction: distribution of the L_1 error as a function of the number of points. □, $H7$; ○, $H5$; △, $W7$; ◇, $W5$.

shock resolving property and the better resolution properties of the compact scheme over the WENO ones. Note that indeed the entropy waves downstream of the shock are in this case captured with $n_p \approx 6$ points per wavelength. However, on finer meshes, which resolve the sine waves with many more points, the performance of WENO and hybrid schemes is similar.

For the purpose of assessing the effect of the switch parameter β and of the type of flux splitting on the quality of the solution, we have performed additional calculations, whose results are reported in Figs. 12 and 13. In Fig. 12 we report the density distribution obtained with the scheme $H7$ for $\beta = 0.4$ and 0.2, which correspond to increasing the number of nodes in the flow field which are treated with the WENO algorithm. The figure shows that, as expected, the scheme becomes more and more dissipative, and its behavior becomes more similar to a pure $W7$ scheme. In particular, the peaks close to the interface between the rarefaction and the entropy waves are smoothed out, while the oscillations at the shocklets become less and less evident, thus indicating that the WENO scheme is now turned on there. However, the results are still better than those reported for a hybrid compact-ENO scheme [1]. The density distribution obtained with the $H7$ algorithm (with $\beta = 0.8$) using the HDLF flux splitting is reported in Fig. 13. A comparison with Fig. 10 demontrates that indeed this type of flux splitting is more dissipative than the LDLF one, even though it is significantly less expensive to compute, with $O(15\%)$ savings in computation time.

5.3. Shock-Vorticity Wave Interaction in 2D

In the present example, which is also taken from Ref. [41], a vorticity wave is made to interact with a $M = 8$ shock wave in a two-dimensional environment. The same test case has been computed, for example, in Refs. [1, 19, 48]. A shock wave is initially located at $x = -1$ and is moving into a gas whose state is defined by

$$\begin{aligned}
\rho(x, y) &= 1, \\
u(x, y) &= -\sqrt{\gamma}\sin\theta\cos(kx\cos\theta + ky\sin\theta), \\
v(x, y) &= \sqrt{\gamma}\cos\theta\cos(kx\cos\theta + ky\sin\theta), \\
p(x, y) &= 1,
\end{aligned}$$

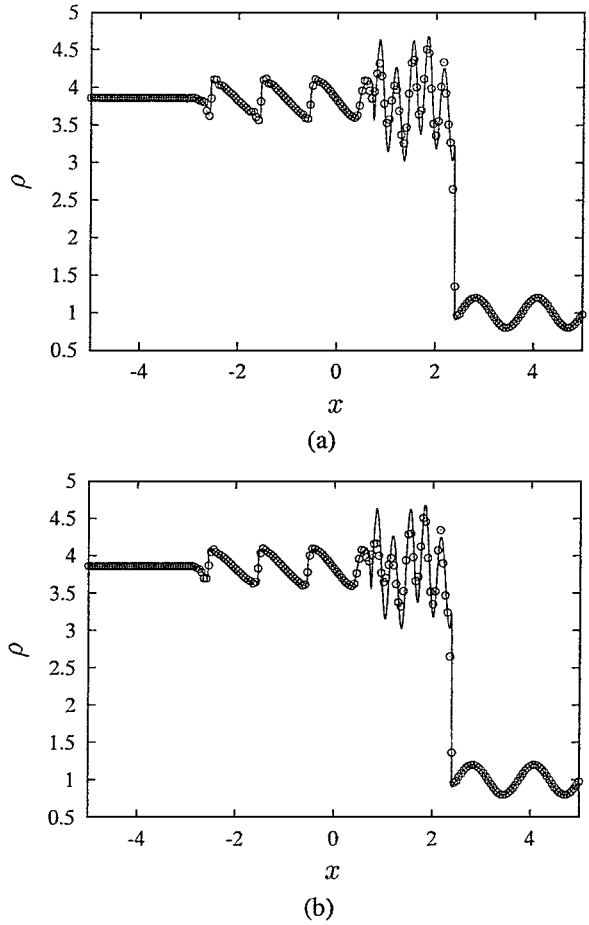

FIG. 12. Shock/entropy wave interaction: distribution of density for $N = 200$ for the $H7$ scheme. (a) $\beta = 0.4$; (b) $\beta = 0.2$. ○, Computed solution; ——, "exact" solution.

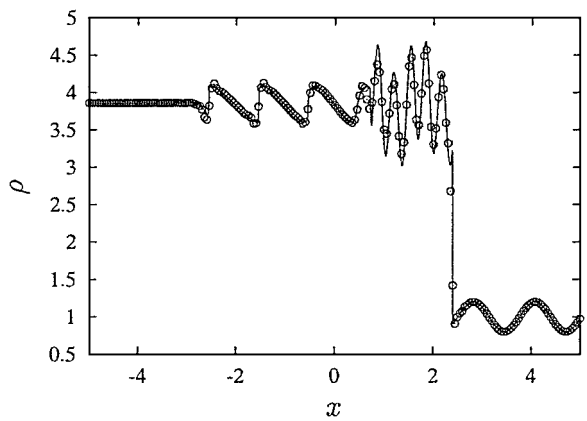

FIG. 13. Shock/entropy wave interaction: distribution of density for $N = 200$ for the $H7$ scheme + HDLF flux splitting formulation ($\beta = 0.8$). ○, Computed solution; ——, "exact" solution.

where $\gamma = 1.4$ is the specific heat ratio, $\theta = \pi/6$ is the angle of the vorticity wave with respect to the shock, and $k = 2\pi$. The initial state downstream of the shock is specified to be uniform and related to the undisturbed upstream flow through the Rankine–Hugoniot jump relations. The problem is solved in the spatial domain $(x, y) \in [-1.5, 1.5] \times [-1, 1]$ and computed up to $t = 0.2$ on a uniformly spaced mesh whose spacing in the coordinate directions is Δx, Δy. Periodic boundary conditions are enforced in the y-direction, while zero time variation is specified at the inflow and the outflow. The time step is kept constant and computed according to

$$\Delta t = \sigma \frac{\Delta t_x \, \Delta t_y}{\Delta t_x + \Delta t_y},$$

where

$$\Delta t_x = \frac{\Delta x}{\max_{i=1,N_x;\, j=1,N_y} (|u_{i,j}| + c_{i,j})},$$

$$\Delta t_y = \frac{\Delta y}{\max_{i=1,N_x;\, j=1,N_y} (|v_{i,j}| + c_{i,j})},$$

and with a Courant number $\sigma = 0.5$. The switch parameter of the hybrid algorithm has been set to a conservative value $\beta = 0.8$ to avoid oscillations to appear past the strong shock.

The results of the study are reported in Figs. 14–16. Two different grids have been considered for the present study: a coarse one consisting of 96×64 nodes and a finer grid, consisting of 192×128 nodes. For the purpose of comparing with an "exact" solution, we have also computed the same test case with the $W7$ scheme on a much finer grid, consisting of 960×640 nodes. In Fig. 14 we report the spatial distribution of the computed density field on the two grids here considered. The "exact" solution consists of a set of acoustic waves moving to the left with respect to the shock wave and a set of vorticity and entropy waves moving more slowly; the two regions are separated by a rather sharp interface, which is clearly observed in the figure at $x \approx 0.55$. The figure shows that all the schemes correctly capture the salient features of the flow; in particular, the acoustic waves, which are associated to longer wavelengths, are well captured even on the coarse mesh, while differences among the various algorithms are discernible in the region close to the shock. In order to analyze the differences in a greater detail, in Fig. 15 we report a close-up (in the proximity of the shock) of the sections of the density field taken at $y = 0$. The figure indicates significant differences in the computed solution on the coarser mesh. It is seen that the $W5$ scheme significantly damps all the extrema, and in particular the entropy waves are very poorly reproduced. A somewhat better behavior of the $H7$ hybrid scheme over the $W7$ algorithm is also observed, at least far from the shock, with a more faithful reproduction of the behavior of the solution close to the acoustic-entropy transition zone. For completeness, in Fig. 16 we also report the computed vorticity field, which also demonstrates that the $H7$ algorithm has a very similar behavior to the $W7$ one, although at a much lower computational cost. Finally, we observe that this test is not particularly challenging with respect to the resolution properties of a numerical scheme, as relatively long wavelength disturbances are involved, and WENO and hybrid schemes perform similarly.

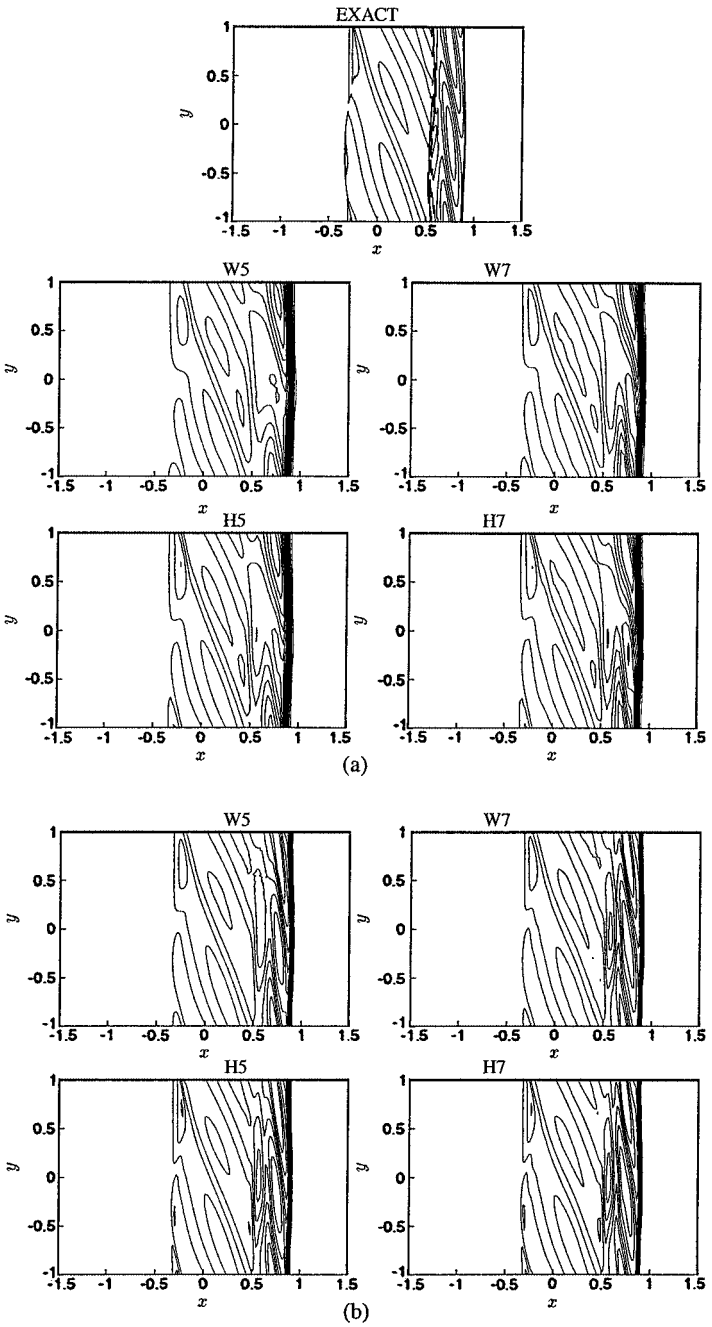

FIG. 14. Shock/vorticity wave interaction: density field. (a) $N_x = 96$, $N_y = 64$; (b) $N_x = 192$, $N_y = 128$. Thirty contour levels from 0.99 to 6.16.

5.4. Shock-Turbulence Interaction in 3D

As a final test of the capabilities of the different numerical schemes here discussed, we present the application to a case of shock-turbulence interaction in three space dimensions. Numerical simulations and analyses of the interaction of a field of isotropic turbulence

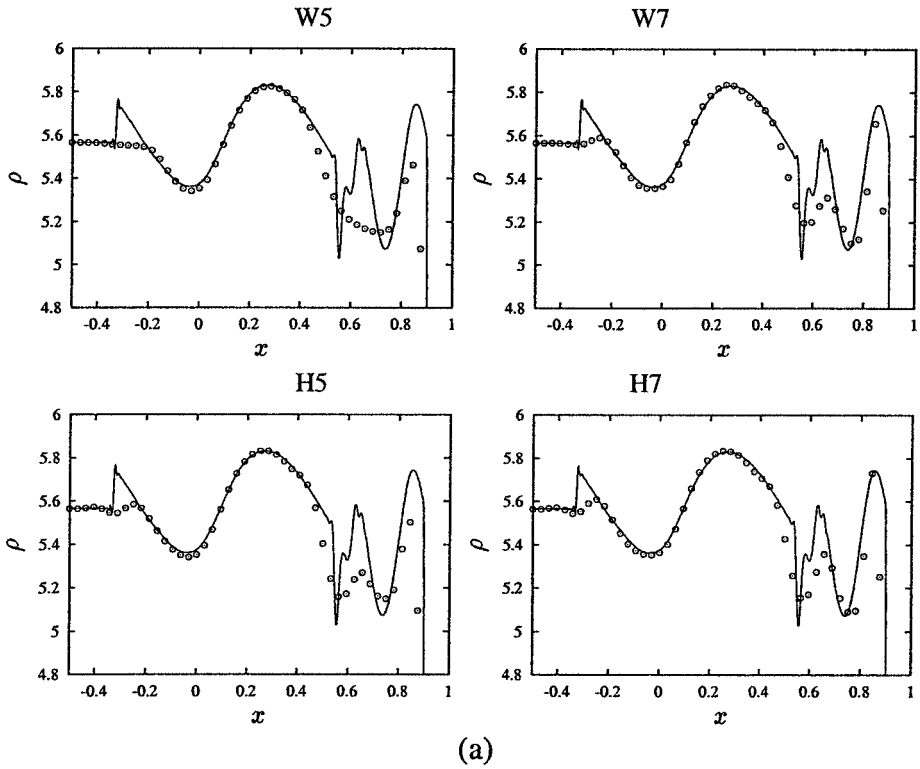

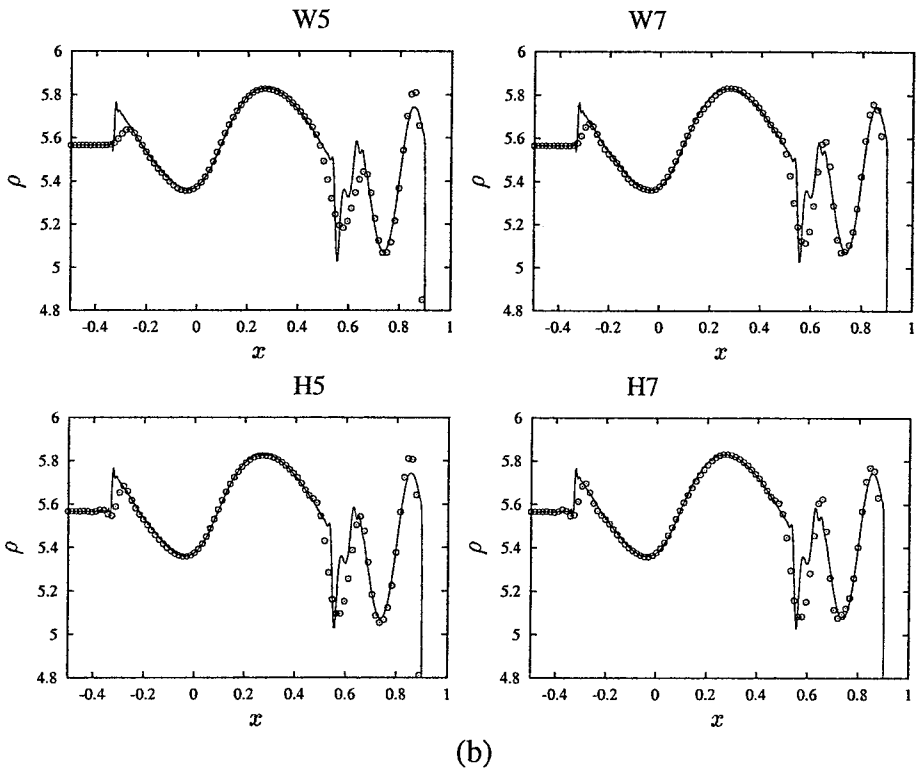

FIG. 15. Shock/vorticity wave interaction: distribution of density along the $y = 0$ section. ○, Computed solution; ——, "exact" solution. (a) $N_x = 96$, $N_y = 64$; (b) $N_x = 192$, $N_y = 128$.

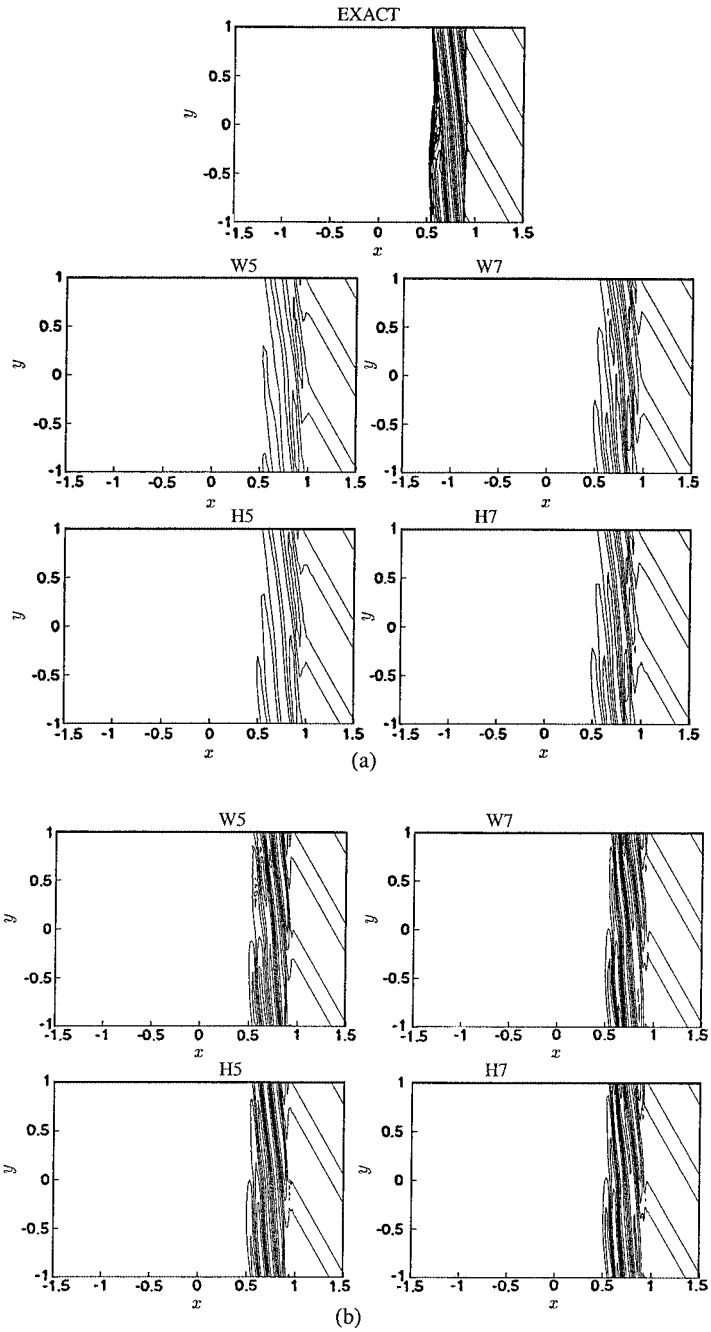

FIG. 16. Shock/vorticity wave interaction: vorticity field. (a) $N_x = 96$, $N_y = 64$; (b) $N_x = 192$, $N_y = 128$. Sixteen contour levels from -100 to 100.

interacting with a planar shock wave have been reported in detail in Refs. [26, 27]. Those authors have considered direct numerical simulations of shock-turbulence interaction and have employed a numerical algorithm based on the use of a sixth-order Padé compact sheme in the smooth regions and of a ENO shock-capturing scheme in the proximity of the shock,

whose location is known a priori. In the present study we consider a test case that has been reported in Ref. [27], consisting in a $M = 2$ shock interacting with a field of compressible isotropic turbulence whose characteristic Mach number is $M_t = 0.108$, and whose energy spectrum is given by

$$E(k) \propto (k/k_0)^4 \exp[-2(k/k_0)^2], \tag{42}$$

where k is the wavenumber in Fourier space, and k_0 is the wavenumber corresponding to the most energetic mode (which is set to $k_0 = 4$ in the simulations here reported). The inflow conditions have been generated by prescribing an isotropic solenoidal velocity field with energy spectrum given by Eq. [42], and zero fluctuations for density and pressure; on the other hand, Lee *et al*. [27] employ a more realistic inflow condition using data from a temporally decaying turbulence simulation. Also note that in order to isolate the effect of the discretization of the convective part of the Navier–Stokes equations on the dynamics of turbulence, we have performed the simulations at zero molecular viscosity, which precludes a quantitative comparison with the results of Ref. [27], which is not our purpose, however. The computational domain is defined by $(x, y, z) \in [-2\pi, 2\pi] \times [0, 2\pi] \times [0, 2\pi]$, and the shock is located at $x = 0$. Periodic boundary conditions are enforced at the y- and z-boundaries, while the locally nonreflecting boundary conditions of Thompson type [34, 43] are implemented at the subsonic outflow boundary, augmented with a buffer zone treatment which is used to gradually drive the flow to the mean conditions downstream of the shock wave. For this purpose the computational mesh (which is uniformly spaced in the region of the computational domain of physical interest) is progressively stretched toward the outflow boundary, and approximately 20% of the grid nodes are put in the buffer region. Damping terms have been added to the right-hand side of the governing equations in the form $\sigma(\mathbf{v} - \mathbf{v}_{target})$, where $\mathbf{v}_{target}$ is the vector of conservative variables for the undisturbed state downstream of the shock. The damping parameter σ smoothly varies from zero at $x = 2\pi$ to unity at the right end of the buffer zone. The combination of grid stretching and the use of driving terms has been shown to be a very efficient way to prevent any spurious wave from reflecting from the outflow [10, 13]. No clustering of grid nodes around the shock waves has been attempted, as was done in Ref. [27]. In particular, two grids have been considered in the study: a finer one, consisting of $160 \times 64 \times 64$ nodes, and a coarser one, consisting of $80 \times 32 \times 32$ nodes. The time step for the Runge–Kutta is held constant throughout the calculation, and the Courant number has been set to $\sigma = 1$. The computation has been advanced up to a large time $t = 64$, after which all the relevant turbulence statistical properties achieved time independence.

For the present test case it is not obviously possible to compare to an "exact" solution, since for the Euler equation an infinite cascade to smaller and smaller scales is expected as the grid is refined, which is only limited by the numerical viscosity of the numerical scheme (see, for example, Ref. [37]). However, on the basis of what has been presented so far, the most reliable solution is expected to be the one obtained with the $H7$ scheme of the fine grid, which is consistent with the indications of the results presented in Figs. 17–21.

The interaction of turbulence with a shock wave generates vortical, entropy, and acoustic disturbances downstream of the shock [7, 35]. We point out that since the turbulence is stationary and homogeneous in the cross-stream directions (y and z) all the statistical data have been obtained by sampling the solution at discrete time intervals and then performing time and space averages in the homogeneity directions. The evolution of the computed

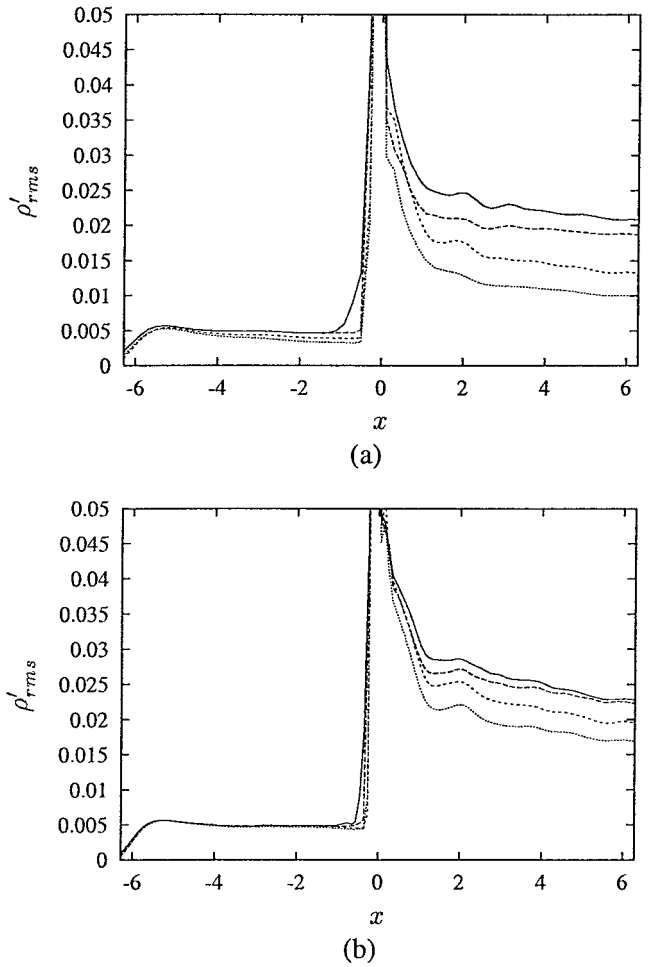

FIG. 17. Shock/turbulence interaction: rms density fluctuations. (a) $N_x = 80$, $N_y = 32$, $N_z = 32$; (b) $N_x = 160$, $N_y = 64$, $N_z = 64$. ——, $H7$; – – –, $H5$; - - -, $W7$; · · · · ·, $W5$.

rms density and pressure fluctuations is reported in Figs. 17 and 18, respectively. Both rms pressure and density start from a zero value at the inflow to reach a nearly constant value after turbulence has rearranged before hitting the shock. After the interaction the levels of rms density and pressure fluctuations are enhanced, consistent with the prediction of linear analyses [6, 32, 35]. After a transition zone, where the flow is dominated by the so-called evenascent waves, the statistical quantities tend to settle down to a nearly constant state and exhibit a return to isotropy [27]. These features are reproduced by all the simulations here reported. However, the schemes $W5$ and $W7$ do exhibit a more dissipative behavior even upstream of the shock (which is more evident on the coarse mesh). The flow downstream of the shock is very sensitive to the numerics. Indeed, the plateau levels predicted by the weighted ENO schemes are considerably lower than those predicted by the corresponding hybrid schemes. The latter schemes provide more reliable results, as confirmed by the analyses of the figures, which indeed show that nearly grid-independent results are obtained for the $H7$ algorithm and to a certain extent also for the $H5$ algorithm. This is particularly

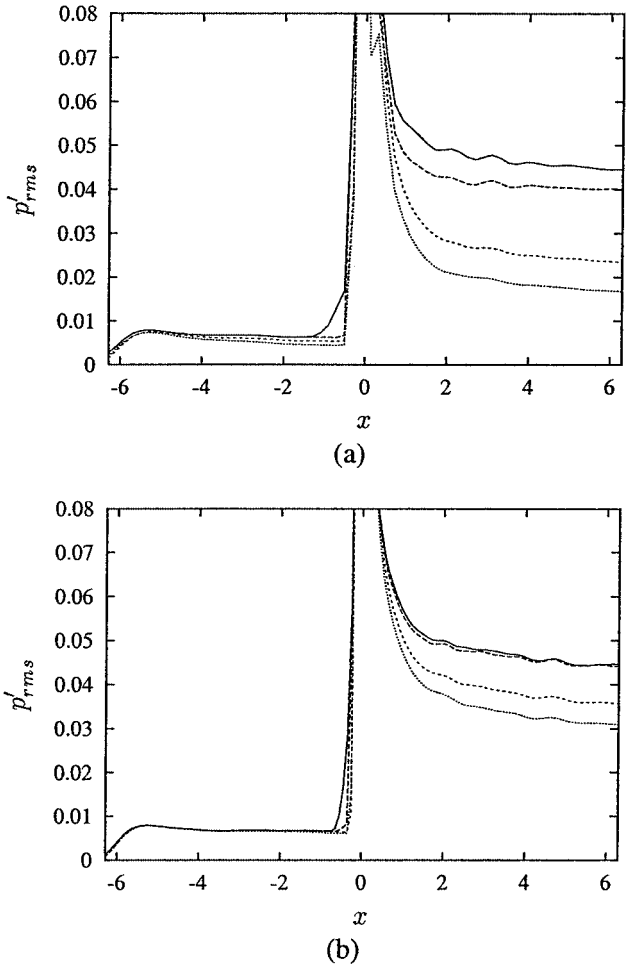

FIG. 18. Shock/turbulence interaction: rms pressure fluctuations. (a) $N_x = 80$, $N_y = 32$, $N_z = 32$; (b) $N_x = 160$, $N_y = 64$, $N_z = 64$. ——, $H7$; – – –, $H5$; - - -, $W7$; · · · · ·, $W5$.

important, as it has been observed that the thermodynamic quantities are particularly sensitive to the grid resolution when using shock-capturing schemes [3, 27], mainly because of the spurious entropy fluctuations generated downstream of a slowly moving shock.

A better insight into the dynamics of the interaction is obtained by looking at the one-dimensional energy spectra [27]. The one-dimensional energy spectrum $E_i(k_j)$ is defined as the spectral energy density of $\overline{u_i'}$ with respect to the wavenumber in the x_j direction k_j and satisfies

$$\overline{u_i'^2} = \int_0^\infty E_i(k_j)\,\mathrm{d}k_j.$$

Since the flow is homogeneous in the y- and z-directions, we have only considered the spectral densities with respect to those coordinate directions; at the same time, since the turbulence is isotropic upstream of the shock and axisymmetric downstream of the shock, it is sufficient to consider only the two independent spectra ($E_2(k_2)$ and $E_3(k_2)$, for example).

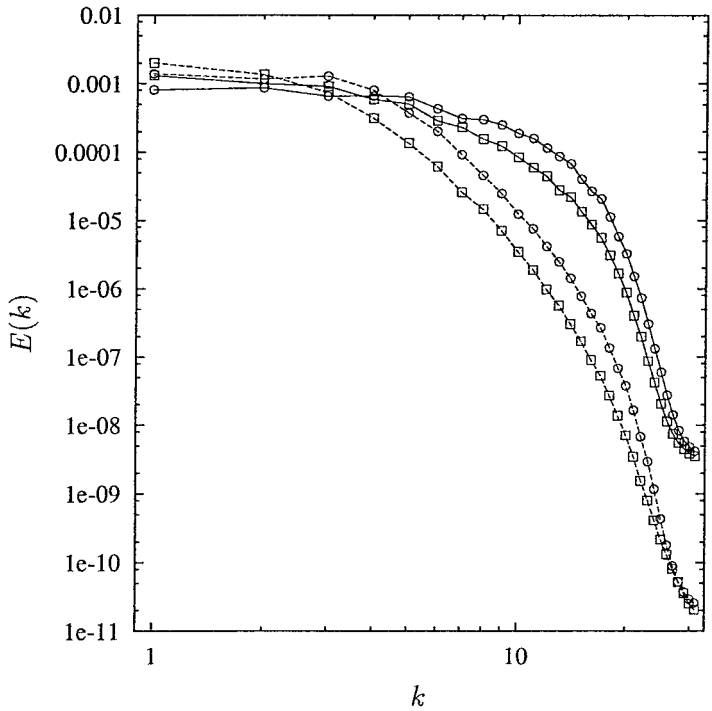

FIG. 19. Shock/turbulence interaction: evolution of one-dimensional spectra, as computed with the $H7$ scheme on the $N_x = 160$, $N_y = 64$, $N_z = 64$ grid. ——, $x = 6$; - - -, $x = -1$. □, $E_2(k_2)$; ○, $E_3(k_2)$.

The computed evolution of the one-dimensional spectra is shown in Fig. 19, where we report the computed spectra (with the $H7$ algorithm on the fine grid) at two locations, the first one immediately upstream of the shock, and the second one toward the end of the well-resolved region. The figure shows that turbulence is mostly amplified at the small wavenumbers, consistently with what observed in Ref. [27], while the large scales are almost unaffected by the interaction.

It is interesting to study how those spectra are affected by the discretization scheme. For this purpose in Figs. 20 and 21 we report the computed one-dimensional spectra upstream and downstream of the shock, respectively. Figure 20 shows that the upstream spectrum is relatively unaffected by the numerics on the fine grid, while differences are observable on the coarse grid, where the weighted ENO schemes prove to be more dissipative. It is also interesting to observe, however, that the hybrid schemes exhibit lower energy levels at the smallest scales (i.e., at the right end of the spectrum). This is due to the peculiar form of the transfer function for the compact upwind scheme, as Fig. 1 clearly demonstrates. The effect of the use of a dissipative scheme is then to provide a numerical dissipation which is most active at the smallest scales, which lie close to the highest resolvable wavenumber. The differences are more evident in the spectra evaluated downstream of the shock, where the intermediate and small scales are greatly enhanced on account of the interaction with the shock wave. Figure 21 actually shows that the hybrid schemes $H5$ and $H7$ yield similar results and exhibit a higherenergy content at the large and intermediate scales. It is also interesting to observe that they exhibit a very different behavior at high wavenumbers: indeed, while the weighted ENO schemes exhibit a cascade of energy up to $n_p = 2$ (i.e., the

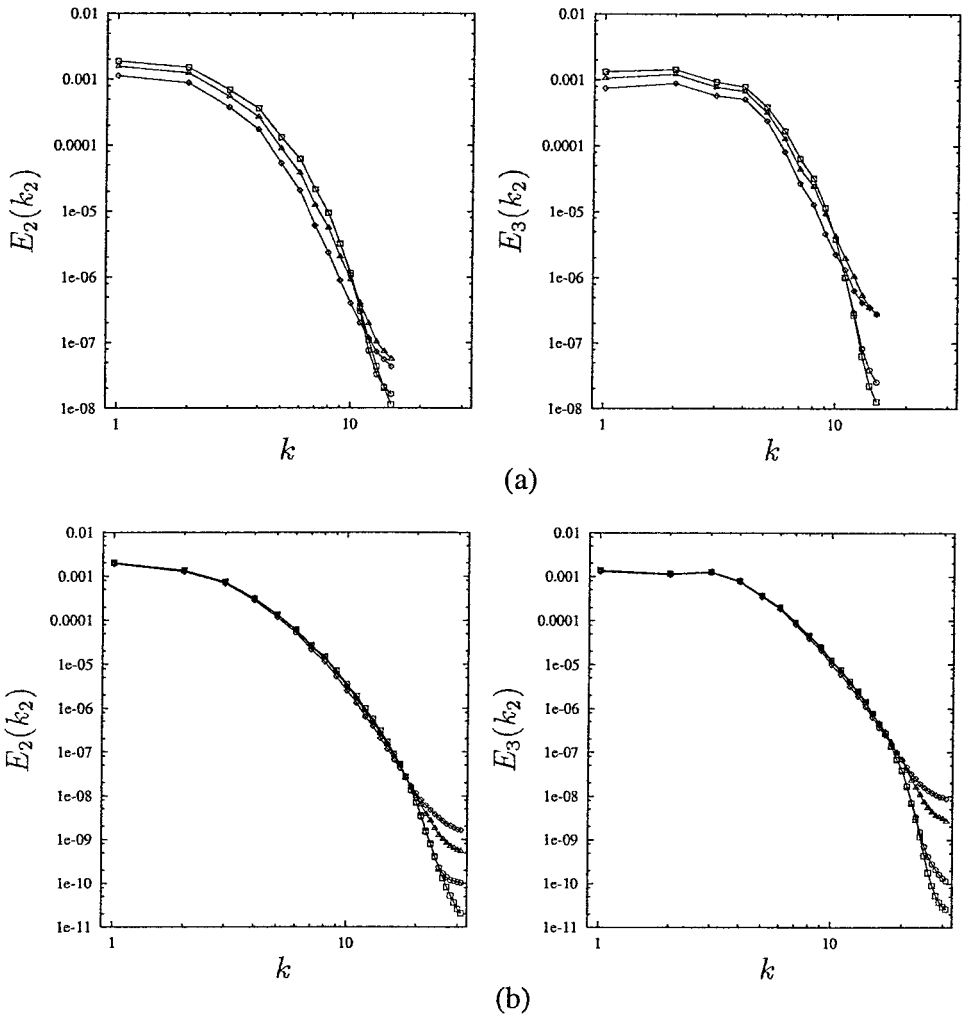

FIG. 20. Shock/turbulence interaction: computed one-dimensional spectra upstream of the shock wave (at $x = -1$). (a) $N_x = 80$, $N_y = 32$, $N_z = 32$; (b) $N_x = 160$, $N_y = 64$, $N_z = 64$. □, $H7$; ○, $H5$; △, $W7$; ◇, $W5$.

highest resolvable wavenumber) the hybrid schemes exhibit a cutoff in the energy spectrum at high wavenumbers, which is observed to occur for waves resolved with $n_p = 3$ points per wavelength. This behavior is consistent with what has been previously observed for the spectral transfer function and is similar to the energy distribution obtained from a low-Reynolds-number direct numerical simulation, while the behavior of the weighted ENO schemes is similar to the one obtained from a high-Reynolds-number large-eddy simulation. An interesting analysis of the behavior of several shock-capturing schemes in the context of numerical simulations of decaying compressible isotropic turbulence at zero molecular viscosity has been presented in Ref. [15], where the approach is referred to as MILES (monotone integrated large-eddy simulation).

In conclusion, while the hybrid schemes do not seem good candidates for a MILES approach, since they do not reproduce an inertial range up to the highest resolvable wavenumber, they are good candidates for the direct numerical simulation of shock-turbulence interaction, since they exhibit a small amount of numerical viscosity at large and intermediate

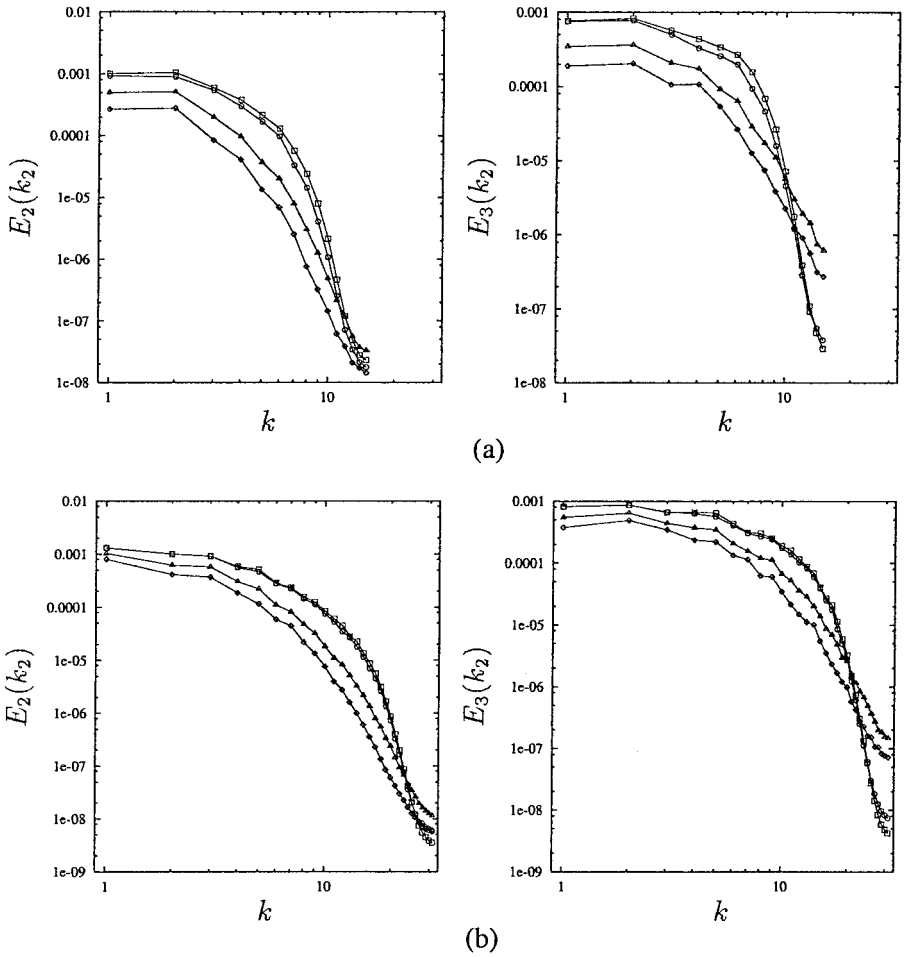

FIG. 21. Shock/turbulence interaction: computed one-dimensional spectra downstream of the shock wave (at $x = 6$). (a) $N_x = 80$, $N_y = 32$, $N_z = 32$; (b) $N_x = 160$, $N_y = 64$, $N_z = 64$. □, $H7$; ○, $H5$; △, $W7$; ◇, $W5$.

scales and exhibit a clear cutoff frequency. On the basis of our results, it is expected that good results for direct numerical simulation can be obtained provided the Kolmogorov scale is resolved with at least three grid points.

6. CONCLUSIONS

In the present paper a hybrid scheme has been developed for the analysis of shock-turbulence interaction problems. The scheme relies on a compact upwind scheme in conservation form to treat smooth regions of the flow field and on a WENO scheme to handle discontinuities. An efficient formulation of the compact upwind scheme has permitted us to obtain excellent resolution properties in the wavenumber space with a narrow stencil, which only requires the inversion of a tridiagonal matrix. A simple switch between the compact and the WENO scheme has been devised (on the basis of the one developed in Ref. [1]) which is based on the undivided differences of the density field. The proposed algorithm has been shown to yield oscillation-free results when shock waves are present, and at the

same time to improve the resolution properties of the algorithm, which is necessary when rich structures are present in the smooth part of the flow field. The results indicate that a conservative formulation of the compact building block guarantees a better resolution of waves, and at the same time the use of a high-order WENO scheme is important for obtaining good performance of the overall algorithm. A test performed on a realistic shock-turbulence interaction problem indicates that the proposed scheme is a good candidate for the direct numerical simulation of such flows.

ACKNOWLEDGMENT

The author thanks Prof. C.-W. Shu for precious suggestions and comments on a draft version of the present paper and for providing the tool to compute the exact solution of the Burgers equation.

REFERENCES

1. N. A. Adams and K. Shariff, A high-resolution hybrid compact-ENO scheme for shock-turbulence interaction problems, *J. Comput. Phys.* **127**, 27 (1996).
2. N. A. Adams, Direct numerical simulation of turbulent compression corner flow, *Theor. Comp. Fluid Dyn.* **12**, 109 (1998).
3. M. Arora and P. L. Roe, On postshock oscillations due to shock capturing schemes in unsteady flows, *J. Comput. Phys.* **130**, 25 (1997).
4. D. Balsara and C.-W. Shu, Monotonicity preserving weighted essentially non-oscillatory schemes with increasingly high order of accuracy, *J. Comput. Phys.* **160**, 405 (2000).
5. M. Carpenter, D. Gottlieb, and C.-W. Shu, On the conservation and convergence to weak solutions of global schemes, *J. Sci. Comput.*, in press.
6. C. T. Chang, Interaction of a plane shock and oblique plane disturbances with special reference to entropy waves, *J. Aero. Sci.* **24**, 675 (1957).
7. B. T. Chu and L. S. G. Kovásznay, Non-linear interactions in a viscous heat-conducting compressible gas, *J. Fluid Mech.* **3**, 494 (1957).
8. B. Cockburn and C.-W. Shu, Nonlinearly stable compact schemes for shock calculation, *SIAM J. Numer. Anal.* **31**, 607 (1994).
9. L. Collatz, *The Numerical Treatment of Differential Equations* (Springer-Verlag, New York, 1966).
10. T. Colonius, S. Lele, and P. Moin, Boundary conditions for direct computation of aerodynamic sound, *AIAA J.* **31**, 1574 (1993).
11. X. Deng and H. Maekawa, Compact high-order accurate nonlinear schemes, *J. Comput. Phys.* **130**, 77 (1997).
12. X. Deng and H. Zhang, Developing high-order weighted compact nonlinear schemes, *J. Comput. Phys.* **165**, 22 (2000).
13. J. B. Freund, Proposed inflow/outflow boundary condition for direct computation of aerodynamic sound, *AIAA J.* **35**, 740 (1997).
14. D. Gaitonde and J. S. Shang, Optimized compact-difference-based finite-volume schemes for linear wave phenomena, *J. Comput. Phys.* **138**, 617 (1997).
15. E. Garnier, M. Mossi, P. Sagaut, P. Comte, and M. Deville, On the use of shock-capturing for large-eddy simulation, *J. Comput. Phys.* **153**, 273 (1999).
16. E. Garnier, P. Sagaut, and M. Deville, A class of explicit ENO filters with application to unsteady flows, *J. Comput. Phys.* **170**, 184 (2001).
17. F. Grasso and S. Pirozzoli, Simulations and analysis of the coupling process of compressible vortex pairs: free evolution and shock induced coupling, *Phys. Fluids* **13**, 1343 (2001).
18. B. Gustafsson, The convergence rate for difference approximations to mixed initial boundary value problems, *Math. Comput.* **29**, 396 (1975).

19. R. Hannapel, T. Hauser, and R. Friedrich, A comparison of ENO and TVD schemes for the computation of shock-turbulence interaction, *J. Comput. Phys.* **121**, 176 (1995).
20. A. Harten, B. Engquist, S. Osher, and S. Chakravarthy, Uniformly high order essentially non oscillatory schemes, III, *J. Comput. Phys.* **71**, 213 (1987).
21. C. Hirsch, *Numerical Computation of Internal and External Flows* (Wiley, New York, 1988).
22. G. S. Jiang and C.-W. Shu, Efficient implementation of weighted ENO schemes, *J. Comput. Phys.* **126**, 202 (1996).
23. L. Jiang, H. Shan, and C. Liu, Weighted compact schemes for shock capturing, *Int. J. Comput. Fluid D.* **15**, 147–155 (2001).
24. M. H. Kobayashi, On a class of Padé finite volume methods, *J. Comput. Phys.* **156**, 137 (1999).
25. Z. Kopal, *Numerical Analysis* (Wiley, New York, 1961).
26. S. Lee, S. K. Lele, and P. Moin, Direct numerical simulation of isotropic turbulence interacting with a weak shock wave, *J. Fluid Mech.* **251**, 533 (1993).
27. S. Lee, S. K. Lele, and P. Moin, Interaction of isotropic turbulence with shock waves: effect of shock strength, *J. Fluid Mech.* **340**, 255 (1997).
28. S. K. Lele, Compact finite difference schemes with spectral-like resolution, *J. Comput. Phys.* **103**, 16 (1992).
29. R. LeVecque, *Numerical Methods for Conservation Laws* (Birkhäuser-Verlag, Basel, 1990).
30. X. D. Liu, S. Osher, and T. Chan, Weighted essentially non-oscillatory schemes, *J. Comput. Phys.* **115**, 200 (1994).
31. D.-K. Mao, A treatment of discontinuities in shock-capturing finite difference methods, *J. Comput. Phys.* **92**, 422 (1991).
32. J. F. McKenzie and L. O. Westphal, Interaction of linear waves with oblique shock waves, *Phys. Fluids* **11**, 2350 (1968).
33. S. Pirozzoli, F. Grasso, and A. D'Andrea, Interaction of a shock wave with two counter-rotating vortices: shock dynamics and sound production, *Phys. Fluids* **13**, 3460 (2001).
34. T. J. Poinsot and S. K. Lele, Boundary conditions for direct simulations of compressible viscous reacting flows, *J. Comput. Phys.* **101**, 104 (1992).
35. H. S. Ribner, *Convection of a Pattern of Vorticity through a Shock Wave*, NACA TN 2864 (1993).
36. A. Rogerson and E. Meiburg, A numerical study of the convergence properties of ENO schemes, *J. Sci. Comput.* **5**, 151 (1990).
37. R. Samtaney and D. I. Pullin, On initial-value and self-similar solutions of the compressible Euler equations, *Phys. Fluids* **8**, 2650 (1996).
38. C.-W. Shu, Numerical experiments on the accuracy of ENO and modified ENO schemes, *J. Sci. Comput.* **5**, 127 (1990).
39. C.-W. Shu, Essentially non-oscillatory and weighted essentially non-oscillatory schemes for hyperbolic conservation laws, in *Advanced Numerical Approximation of Nonlinear Hyperbolic Equations*, Lecture Notes in Mathematics edited by B. Cockburn, C. Johnson, C.-W. Shu, E. Tadmor, and A. Quarteroni (Springer-Verlag, Berlin, 1998), Vol. 1697, p. 425.
40. C.-W. Shu and S. Osher, Efficient implementation of essentially non-oscillatory shock-capturing schemes, *J. Comput. Phys.* **77**, 439 (1988).
41. C.-W. Shu and S. Osher, Efficient implementation of essentially non-oscillatory shock-capturing schemes II, *J. Comput. Phys.* **83**, 32 (1989).
42. C. K. W. Tam and J. C. Webb, Dispersion-relation-preserving finite difference schemes for computational acoustics, *J. Comput. Phys.* **107**, 262 (1993).
43. K. W. Thompson, Time dependent boundary conditions for hyperbolic systems, *J. Comput. Phys.* **68**, 1 (1987).
44. A. I. Tolstykh and M. V. Lipavskii, On performance of methods with third- and fifth-order compact upwind differencing, *J. Comput. Phys.* **140**, 205 (1998).
45. R. Vichnevetsky and J. B. Bowles, *Fourier Analysis of Numerical Approximations of Hyperbolic Equations* (SIAM, Philadelphia, 1982).

46. Z. J. Wang and R. F. Chen, *Optimized Weighted Essentially Non-Oscillatory Schemes for Computational Aeroacoustics*, AIAA Paper 2001–1101 (2001).
47. V. G. Weirs and G. V. Candler, *Optimization of Weighed ENO Schemes for DNS of Compressible Turbulence*, AIAA Paper 97–1940 (1997).
48. T. A. Zang, M. Y. Hussaini, and D. M. Bushnell, Numerical computations of turbulence amplification in shock-wave interactions, *AIAA J.* **22**, 13 (1984).
49. M. Zhuang and R. F. Cheng, Optimized upwind dispersion-relation-preserving finite difference schemes for computational aeroacoustics, *AIAA J.* **36**, 2146 (1998).
50. H. C. Yee, N. D. Sandham, and M. J. Djomehri, Low-dissipative high-order shock-capturing methods using characteristic-based filters, *J. Comput. Phys.* **150**, 199 (1999).